



Numerical and analytical modeling of unsteady viscoelastic flows: The start-up and pulsating test case problems

A.S.R. Duarte^a, A.I.P. Miranda^b, P.J. Oliveira^{a,*}

^a Departamento de Engenharia Electromecânica, Unidade de Materiais Têxteis e Papeleiros, Universidade da Beira Interior, 6201-001 Covilhã, Portugal

^b Departamento de Matemática/Informática, Universidade da Beira Interior, 6201-001 Covilhã, Portugal

ARTICLE INFO

Article history:

Received 23 August 2007

Received in revised form 8 April 2008

Accepted 22 April 2008

Keywords:

Time-dependent viscoelastic flows

Oscillating flow

Start-up flow

Analytical solution

ABSTRACT

In this paper two test cases adequate for the assessment of viscoelastic flow codes under unsteady flow conditions are investigated. For one of them an analytical solution is also derived.

First, the start-up of planar Poiseuille flow between two parallel plates was tackled. For upper-convected Maxwell and Oldroyd-B models there exist analytical solutions making it possible to evaluate exactly the discretization errors of the transient numerical method. Good agreement was found between the present numerical results and those analytical solutions, especially for “shock” propagation. For the UCM fluid, small numerical oscillations were observed at points where the time derivative of velocity was discontinuous, but for the Oldroyd-B fluid a smooth development of the transient evolution was obtained. Results with the PTT model without solvent viscosity and the FENE fluids were also obtained and, as expected, the behaviour was similar to that found for the UCM and Oldroyd-B fluids, respectively.

Then, a pulsating flow problem was studied. In this test case the flow is generated by a periodic pressure-gradient superimposed on a constant Poiseuille flow. The analytical solution for pulsatile Oldroyd-B flow in a channel was derived as part of the work and, again, difficulties in obtaining accurate numerical solutions with the UCM model were encountered, being necessary to employ extremely refined meshes. For the Oldroyd-B fluid no difficulties were found and the accuracy tended to improve with larger solvent viscosity parameter.

© 2008 Elsevier B.V. All rights reserved.

1. Introduction

Unsteady flows are gradually becoming the main focus of attention in computational rheology studies. Over the past two decades stable numerical algorithms were developed and optimized for the solution of steady viscoelastic flow problems [1,2]. Currently, the attention has largely been diverted towards the solution of unsteady flow problems which are relevant not only because many actual flows of interest occur in variable regimes, as exemplified by injection and blow molding, purely extensional flows, or blood flow in arteries and veins, but also due to the tendency of non-Newtonian systems to develop time-dependent instabilities.

As a consequence, there has been a growing number of works devoted to applying time marching procedures, typically used to obtain steady state solutions, to the calculations of actual time-dependent flows, with either finite volume methods [3–5], finite element methods [2,6], with a combination of finite element and finite volume methods [7,8], or even with spectral element meth-

ods [9,10]. This is merely an illustrative list which is not meant to be exhaustive, and many other works have been published dealing with unsteady flows of viscoelastic liquids that may even not follow differential constitutive equations; the backward-tracking Lagrangian method [11] for micro–macro simulations being a good example of such efforts. Also, linear stability analysis of flows subject to temporal instabilities have been conducted and we mention here the works of Keiller [12,13] which will be elaborated below. In spite of these and other works on time-dependent non-Newtonian flows, it is a fair statement, corroborated by others [8,10], that much of the effort of the community has been on solving steady flows and is now more directed towards unsteady flows.

A prerequisite before embarking into the simulation of complex time-dependent flows is the development of a set of sufficiently simple test cases adequate to assess the numerical behaviour of existing codes and, to a large extent, useful time-dependent test cases are missing. In this paper, a detailed numerical study of two test problems involving viscoelastic flows in variable regime will be presented: start-up and pulsating flows in a channel. While the start-up flow is a well-established test problem used by many workers as discussed below, the pulsating flow in a plane channel is a new proposition that we advance in this paper. These

* Corresponding author.

E-mail address: pjpo@ubi.pt (P.J. Oliveira).

problems are solved by application of the numerical simulation program developed by Oliveira et al. [14], based on a multidimensional finite volume formulation which was originally prepared to solve steady viscoelastic flow problems [14] and was later extended to unsteady viscoelastic flows with some degree of complexity [4], such as prediction of viscoelastic vortex shedding behind cylinders. Here we take a step back, from those relatively complex geometries to (apparently) simpler 1D cases, and have adapted the method to solve effectively simple one-dimensional, time-dependent flow problems. These test problems are useful as benchmark cases because they possess analytical solutions thus allowing exact evaluation of discretization errors. In addition, with the test cases here proposed it is possible not only to assess discretization errors but also lagging-errors resulting from the sequential treatment of the equations (momentum and constitutive).

The numerical simulation program was first applied to the benchmark problem of the start-up of planar Poiseuille flow between two parallel plates, which has been used in many recent studies, e.g. [3,5,7–10,15]. This time-dependent transient flow is driven by the instantaneous application of a spatially constant pressure gradient to a fluid initially at rest. With the further assumption that the resulting flow is fully developed it becomes possible to derive an analytical solution to the governing equations. For Newtonian fluids, this solution is well known and is described in several books (e.g. White [16]); for non-Newtonian fluids obeying Maxwell and Oldroyd-B constitutive equations the analytical solution was given by Waters and King [17]. Thus, results from the analytical solution and numerical simulations could be compared for different values of the elasticity number and, through the use of successively refined meshes and progressively smaller time steps, a study was made on how those discretization errors decayed.

In two works most closely related to the present effort, Xue et al. [5] and Van Os and Phillips [10] have carried out thorough investigations on the accuracy and stability of temporal algorithms in the context of, respectively, the finite volume and the finite spectral element methods, with both studies using the start-up flow as test case. However, the approach followed in these studies to set up the start-up flow was different: in Xue et al. a constant pressure difference was prescribed and the flow (apparently) solved for a 1D slice of cells, as we have done here; in Van Os and Phillips the full 2D channel was simulated with the known analytical solution of Waters and King imposed at inlet and outlet. In addition, Van Os and Phillips were more concerned with the stability of various versions and solution algorithms of their spectral element method, and the case considered was basically the Oldroyd-B fluid with $\beta = 1/9$; accuracy was not an issue and the more difficult UCM fluid was not considered. On the other hand, Xue et al. examined the time accuracy of their various implementations of a finite volume algorithm (explicit or implicit; SIMPLE, PISO or SIMPLER pressure-correction algorithms) for the Oldroyd-B with $\beta = 1/9$ on a rather coarse mesh ($NY = 10$), while velocity profiles were graphically compared with the analytical solution for the UCM at two values of elasticity ($E = 0.4$ and 40) on a more refined mesh ($NY = 50$), but in all these cases the order of convergence with Δy and Δt was not established. Webster et al. [8] have given more details for the Oldroyd-B $\beta = 1/9$ and demonstrated convergence rates of $\Delta t^{1.3}$ and Δy^2 , based on local point-wise velocity values, with their FV/FE method at $Wi = 4/3$. It will be clear from the present study, and indeed it was already plain from Xue et al. who in Section 5.1 write “in the purely elastic case some inherent difficulties for transient numerical analysis have arisen”, that the UCM is much more difficult than the Oldroyd-B model in terms of obtaining accurate time-dependent numerical solutions, unless the β parameter of the Oldroyd-B becomes smaller than about 0.001. Hence, from this short review, the question of establishing the rate of convergence

of numerical algorithms for time varying flows of Oldroyd-B and UCM-like fluids is still open, and this is the purpose of the present study, not only with the start-up flow used in those previous works, but also with the new problem here proposed of the pulsating UCM and Oldroyd-B flows.

It is relevant here to mention the linear stability analysis of Keiller [12] for plane Couette flow of UCM fluids. He found that when the problem is solved in a 2D domain the critical Weissenberg number (Wi) above which a finite-difference method becomes unstable scales with the ratio of the mesh spacings, that is $Wi_{crit} \sim \Delta x/\Delta y$ where x is the streamwise direction and y the transverse, velocity gradient direction. In a later work dealing with Poiseuille flow [13], instead of the simpler pressure-gradient free Couette case, the same type of limiting Wi criterion was found for a particular finite-difference scheme but not for an alternative one where apparently the near-wall node was treated more implicitly. Fietier and Deville [9], with a spectral method, did not find the same sort of scaling in their simulations of plane start-up flow of Oldroyd-B fluids; Van Os and Phillips [10] probed various channel lengths and spectral element resolutions and reported that the maximum attainable Wi decreased when $\Delta x = 1/9$ is reduced, but they do not substantiate on Keiller findings, rather they correlate the diminution of We_{crit} with refinement of discretization size, a well-known outcome (e.g. Keunings [18]). In the present study we also cannot confirm that the critical Wi scales with $\Delta x/\Delta y$ since we use only a vertical row of cells (along y), that is, we effectively solve the 1D equations using a 2D procedure (cyclic boundary conditions are applied on the two faces of that vertical row of cells) and as a consequence the Δx cancels out from the final algebraic equations (our results do not depend on the assumed streamwise domain size). However some preliminary simulations using the 2D domain with imposed inlet analytical profiles do suggest that Keller's result is valid, a matter left for future research.

Although the UCM and Oldroyd-B models are able to describe some of the elastic characteristics of actual macromolecular fluids they have known limitations. In this work, more complex models were also considered, namely the Phan-Thien–Tanner (PTT) model [19,20], based on network theory, the finite extensible non-linear elastic (FENE) model, based on kinetic theory [21], and the constant-viscosity FENE version of Chilcott and Rallison known as FENE-CR [22]. These models present the desirable features of shear-thinning and finite elongational viscosity which are not accounted for in UCM and Oldroyd-B models. As will be seen, the constitutive equation used to describe the fluid properties has a strong impact on the results for velocity and stress evolution as well as on the method stability, as already pointed out in previous studies (e.g. [10]).

The other benchmark test problem here studied is a viscoelastic pulsating periodic flow resulting from the application of a pressure gradient which varies sinusoidally in time. In contrast to the start-up problem, this has been scarcely used as a test case in numerical calculations in computational rheology; most of the existing literature is focused on the theoretical treatment of viscoelastic pulsating flows in straight pipes with circular cross-section [23,24], recently extended to curved pipes [25]. A first and main motivation for this problem is to have a flow which is not dominated by the initial conditions and will not develop shear stress fronts, with velocity gradient discontinuities as in the start-up flow case. A second motivation is related with our interest in future simulations of blood flow behaviour, which is unsteady (although not sinusoidal) and viscoelastic, as shown in the recent study of Owens [26] where a FENE-type equation is proposed. Of course, the effort of using elaborated constitutive equations for blood flow like those of [26] has to be left for future investigations. An analytical solution for the velocity and stress distribution of UCM and Oldroyd-B models

under sinusoidal pulsating conditions was obtained as part of the work. This will be useful for the assessment of numerical methods.

2. Governing equations

In this section, the basic conservation equations for isothermal and incompressible flows are presented as well as the constitutive relations for the UCM, Oldroyd-B, PTT and FENE-CR models. Conservation of mass and linear momentum in the absence of body forces is expressed by:

$$\nabla \cdot \mathbf{u} = 0 \quad \text{and} \quad \rho \left(\frac{D\mathbf{u}}{Dt} \right) = -\nabla p + \nabla \cdot \boldsymbol{\tau}_{\text{tot}} \quad (1)$$

where \mathbf{u} is the local velocity vector with components u and v corresponding to the Cartesian coordinates x and y , respectively. Fully established conditions in a long planar channel imply $\partial u / \partial x = 0$ and $v = 0$; hence, the continuity equation is identically satisfied and the momentum equation for a Newtonian fluid with a constant viscosity μ can be simplified to:

$$\rho \frac{\partial u}{\partial t} = -\frac{dp}{dx} + \mu \frac{\partial^2 u}{\partial y^2} \quad (2)$$

However, for a viscoelastic fluid the extra-stress tensor, $\boldsymbol{\tau}_{\text{tot}}$, cannot be easily substituted by velocity gradients. This tensor will be specified by a third equation that determines the rheological viscoelastic behaviour of the fluid. In general $\boldsymbol{\tau}_{\text{tot}}$ can be thought as being composed by a Newtonian (solvent) component, with viscosity η_s , and an additional elastic component $\boldsymbol{\tau}$. So the conservation of linear momentum for a viscoelastic fluid is written here under fully developed conditions as

$$\rho \frac{\partial u}{\partial t} = -\frac{dp}{dx} + \frac{\partial(\tau_{xy})_{\text{tot}}}{\partial y} = -\frac{dp}{dx} + \eta_s \frac{\partial^2 u}{\partial y^2} + \frac{\partial \tau_{xy}}{\partial y} \quad (3)$$

In these equations ρ , p and t are the fluid density (assumed constant), pressure and time, respectively.

Four differential rheological models are used along the paper and the constitutive equation for all models can be written as:

$$\lambda \overset{\nabla}{\boldsymbol{\tau}} + f \boldsymbol{\tau} = 2f' \eta_p \mathbf{D} \quad (4)$$

where λ is the relaxation time of the fluid, f and f' are functions of invariants of $\boldsymbol{\tau}$ that enable to discriminate among the models, η_p is the zero-shear rate polymer contribution to the viscosity, \mathbf{D} the deformation rate tensor and $\overset{\nabla}{\boldsymbol{\tau}}$ is the upper-convected time derivative of the stress tensor, defined as:

$$\overset{\nabla}{\boldsymbol{\tau}} = \frac{\partial \boldsymbol{\tau}}{\partial t} + (\mathbf{u} \cdot \nabla) \boldsymbol{\tau} - \boldsymbol{\tau} \cdot \nabla \mathbf{u} - (\nabla \mathbf{u})^T \cdot \boldsymbol{\tau} \quad (5)$$

The relaxation time gives an indication of the magnitude of the elastic nature of the fluid. As the relaxation time increases, so does the fluid elasticity and a value of zero retrieves the Newtonian constitutive equation. The solvent and polymer viscosities η_s and η_p are related in the following manner:

$$\eta_0 = \eta_s + \eta_p, \quad \beta = \frac{\eta_s}{\eta_0} = \frac{\lambda_r}{\lambda} \quad (6)$$

where η_0 is the total zero-shear rate viscosity and λ_r the retardation time of the fluid. The functions f and f' are unity for both the upper-convected Maxwell (UCM) and Oldroyd-B models ($f=f'=1$). For the UCM, the solvent viscosity ratio is zero ($\beta=0$) and so it is a model devoid of any explicit diffusion term in the momentum equation. Although the UCM is the simplest differential model incorporating elastic effects it is also the hardest in terms of numerical calculations. For the Oldroyd-B model, $\beta \neq 0$ and it becomes equivalent to a linear combination of the UCM model and the Newtonian model.

Shear-thinning characteristics of the PTT and FENE-CR models are controlled by non-trivial functions f and f' . The expression here employed for the stress function in the PTT model is the linearized form given in the original paper [20]:

$$f = 1 + \left(\frac{\varepsilon \lambda}{\eta_p} \right) \text{tr}(\boldsymbol{\tau}), \quad f' = 1 \quad (7)$$

where ε is a parameter related to the elongational behaviour of the model and $\text{tr}(\boldsymbol{\tau})$ is the trace of the stress tensor. The PTT model was derived from network theory and predicts a bounded extensional viscosity with a maximum value proportional to $1/\varepsilon$, while the UCM and Oldroyd-B models yield an unbounded elongational viscosity at a finite strain rate of $\lambda \dot{\varepsilon} = 0.5$. It degenerates into the Oldroyd-B model when $\varepsilon=0$, and the UCM if $\eta_s = \varepsilon = 0$.

The FENE family of models is “molecular” based and was developed from kinetic theory by Bird et al. [21]. The Chilcott and Rallison [22] version yields a constant-shear viscosity fluid with finite spring extensibility, and corresponds to putting:

$$f = \frac{(L^2 + (\lambda/\eta_p) \text{tr}(\boldsymbol{\tau}))}{(L^2 - 3)}, \quad f' = f \quad (8)$$

where the parameter L^2 is a measure of the stretch of the basic dumbbell constituents in the molecular representation of the model fluid.

The simplified forms of the constitutive equations for the fully developed planar flows under consideration here will be given in Section 4.

3. Numerical method

As already pointed out in Section 1, the computer program is a quite general simulation tool based on a fully implicit finite-volume method and has been used in the calculation of two- and three-dimensional flows of fluids that follow differential viscoelastic constitutive models. One of the purposes of the present study is to assess the ability of this general code in relatively simple time-dependent problems for which analytical solutions are either available or can be derived.

The governing equations given in Section 2 are integrated in space over the control volumes (cells) forming the computational mesh, and in time, over small time steps Δt , so that sets of linearized algebraic equations are obtained. The method uses a non-staggered grid arrangement, in which all dependent variables are located at the centre of the control volumes, thus simplifying the adoption of general curvilinear coordinates required in more complex problems. As a consequence, special procedures are required to ensure the pressure/velocity coupling and velocity/stress coupling, which were described in Oliveira et al. [14].

The linearized algebraic equations obtained have the general form:

$$a_P^\phi \phi_P = \sum_F a_F^\phi \phi_F + S^\phi \quad (9)$$

to be solved for the velocity or stress components ($\phi = \mathbf{u}$ or $\phi = \boldsymbol{\tau}$). In these equations a_P are coefficients, accounting for convection and diffusion influences, S are source terms encompassing all terms not included in the coefficients, the index P denotes the cell in question and F its neighbour cells. For the present problems a single row of cells aligned with the y -axis (see Fig. 1) will be sufficient due to the fully developed conditions, so the index F varies from one to two only, to indicate the cell immediately above (+ y) and below (- y) any given cell P .

Equation sets like Eq. (9) can be viewed under a matrix form $Ax=b$ typical of linear equation systems and are solved by a bi-

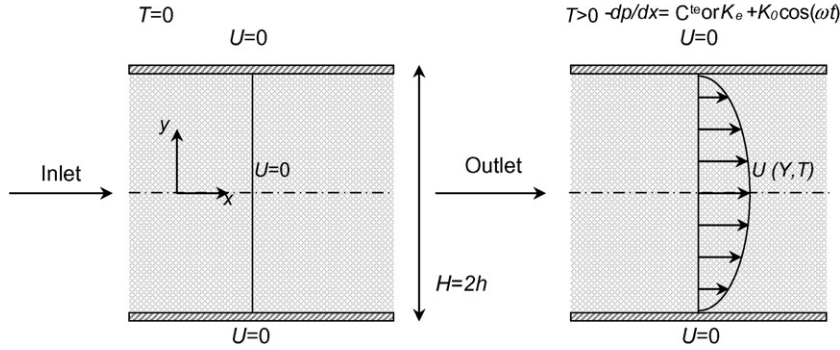


Fig. 1. Schematic representation of the geometry for the start-up and pulsating flow problems.

conjugate gradient solver. The spatial discretization method is second-order accurate [14] and the temporal discretization is also accomplished through a second-order three-time level method [4]:

$$\frac{\partial \phi}{\partial t} = \frac{3\phi^{n+1} - 4\phi^n + \phi^{n-1}}{2\Delta t} \quad (10)$$

where index n denotes time levels. This three-time level method, analogous to the BDF2 (backward differentiation formula) scheme of Van Os and Phillips [10], offers improved accuracy compared to the implicit Euler method which is only first-order accurate in time (e.g. [5]).

As commented before, the full features of the simulation code are not required for the present problems and suffices to solve discretization Eq. (9) for the axial velocity component u , and the shear and normal stress components τ_{xy} and τ_{xx} . These dependent variables are function only of y and t . The pressure gradient is given and therefore the velocity/pressure algorithm is effectively switched off. Boundary conditions are applied at walls, where a no-slip condition is assumed, and at inlet, where the initial fields are prescribed (usually zero velocity and stresses). At every iteration, the velocity and stress components calculated at the CVs centres are extrapolated to the outlet plane; then, because of the single row of cells, those outlet values are assigned to the inlet plane, and the calculation proceeds. In this way, fully developed conditions $\partial/\partial x = 0$ are obtained, provided the iterations within a time step are converged to a tight tolerance (10^{-4} or 10^{-6} in the L1 norm of the residuals).

Specification of stress at solid walls requires further attention. An important finding during the course of the present study is that the simple procedure used in previous works, in which a local viscometric flow is assumed and the stress components at the wall are prescribed on the basis of corresponding analytical solutions, gives rise to a deterioration of accuracy and it is better to obtain the stress directly from the momentum equations. For the Oldroyd-B fluid the previous method for boundary conditions would give the wall shear stress as

$$\tau_{xy} = \eta_0 \frac{\partial u}{\partial y} \Rightarrow (\tau_{xy})_w = \eta_0 \frac{u_w - u_p}{\Delta y/2} \quad (11)$$

where w denotes the wall node and P the adjacent internal node at a distance $\Delta y/2$ from the wall. If the wall is fixed, then $u_w = 0$. For the shear-thinning models, the expression is the same but the viscosity is calculated analytically based on the local shear rate ($\eta(\dot{\gamma})$). In the new method of implementing the boundary conditions, the wall shear stress is calculated directly from Eq. (3) giving:

$$-\frac{dp}{dx} + \frac{\partial \tau_{xy}}{\partial y} = 0 \Rightarrow (\tau_{xy})_w = (\tau_{xy})_p + \left(\frac{dp}{dx}\right)_p \frac{\Delta y}{2}. \quad (12)$$

where the viscous part is omitted for clarity. For the present problems the pressure gradient is known and may vary only with time.

In general dp/dx is the pressure gradient parallel to the wall plane evaluated at the nearest centre of cell position P .

4. Problems description and analytical solutions

We deal separately with the two problems: the start-up flow and the pulsating flow of viscoelastic fluids in a planar channel. The simulations presented in this paper are valid for flow in a two-dimensional channel bounded by two parallel plates separated by height $2h$ in the (x,y) plane, with y representing the transverse direction according to Fig. 1. The task is to determine how the velocity and stresses in the channel evolve in time until a stationary regime is reached.

4.1. Start-up flow

The transient flow resulting from the sudden application of a spatially constant pressure gradient to a fluid initially at rest is a good example of an actual time-dependent flow problem amenable to exact mathematical analysis. For viscoelastic fluids, this problem was initially studied by Waters and King [17] who determined the analytical solution for start-up of planar Poiseuille flow of UCM and Oldroyd-B models.

For the Newtonian case the equation to be solved is Eq. (2) which, with non-dimensional variables

$$Y = \frac{y}{h}, \quad T = \frac{\mu}{\rho h^2} t, \quad U = \frac{u}{\bar{u}_\infty}, \quad (13)$$

where the average steady-state velocity ($t \rightarrow \infty$) is $\bar{u}_\infty = -h^2 dp/dx / 3\mu$ has the following analytical solution given in many books (e.g. White [16]):

$$U(T, Y) = 1.5(1.0 - Y^2) - 48 \sum_{n'=1}^{\infty} \left[n'^{-3} \sin\left(\frac{1}{2}n'(1+Y)\right) e^{-(n'^2 T/4)} \right] \quad (14)$$

where $n = (2n' - 1)\pi$. We note again that here the non-dimensional time T is based on a diffusion time scale $t_D = \rho h^2 / \mu$.

For viscoelastic fluid the equation of motion is now Eq. (3) and in the case of the Oldroyd-B model (Eq. (4) with $f=f' = 1$) under fully developed condition, $\tau_{yy} = 0$, the shear stress equation becomes:

$$\tau_{xy} + \lambda \frac{\partial \tau_{xy}}{\partial t} = \eta_p \frac{\partial u}{\partial y}, \quad (15)$$

After combining Eq. (15) with Eq. (3) in order to eliminate the stress, we have:

$$\left(1 + \lambda \frac{\partial}{\partial t}\right) \frac{\partial u}{\partial t} = -\frac{1}{\rho} \left(1 + \lambda \frac{\partial}{\partial t}\right) \frac{dp}{dx} + \frac{\eta_0}{\rho} \left(1 + \lambda \frac{\partial}{\partial t}\right) \frac{\partial^2 u}{\partial y^2}. \quad (16)$$

whose solution for a constant dp/dx is [17]:

$$U(T, Y) = 1.5(1.0 - Y^2) - 48 \sum_{n'=1}^{\infty} \left[n^{-3} \sin\left(\frac{1}{2}n(1+Y)\right) e^{-(\alpha n T/2)} G(T) \right], \quad (17)$$

where

$$G(T) = \cosh\left(\frac{1}{2}\beta_n T\right) + \frac{\gamma_n}{\beta_n} \sinh\left(\frac{1}{2}\beta_n T\right), \quad (18)$$

and

$$n = (2n' - 1)\pi, \quad \alpha_n = 1 + \frac{1}{4}\beta_n E n^2, \quad \beta_n = \sqrt{\alpha_n^2 - E n^2}, \quad (19)$$

$$\gamma_n = 1 - \frac{1}{4}(2 - \beta)E n^2. \quad (19)$$

Eq. (18) is only valid for a real β_n ; if $\alpha_n^2 - E n^2 < 0$ then the function $G(T)$ becomes:

$$G(T) = \cos\left(\frac{\beta_n T}{2}\right) + \frac{\gamma_n}{\beta_n} \sin\left(\frac{\beta_n T}{2}\right) \quad (20)$$

where now $\beta_n = \sqrt{E n^2 - \alpha_n^2}$. In the above expressions E is the elasticity number defined by the ratio of Weissenberg (Wi) and Reynolds (Re) numbers:

$$Wi = \frac{\lambda \bar{u}_{\infty}}{h}, \quad Re = \frac{\rho \bar{u}_{\infty} h}{\eta_0}, \quad E = \frac{Wi}{Re} = \frac{\lambda \eta_0}{\rho h^2}. \quad (21)$$

The viscoelastic solution, Eq. (17), is rather similar to the Newtonian solution, Eq. (14), but it is noted that the time scale is now the relaxation time of the fluid, $T = t/\lambda$.

4.2. Pulsating flow

For the pulsating flow problem we have the same geometry of Fig. 1 but now the fluid is subject to a pressure gradient varying sinusoidally in time, according to

$$-\frac{1}{\rho} \frac{dp}{dx} = K_S + K_O \cos(\omega t) \quad (22)$$

where ρK_O is the amplitude and ω the frequency of the oscillatory pressure gradient superimposed onto a stationary pressure gradient of magnitude ρK_S . Linear period and angular frequency are related by the usual expression $T_0 = 2\pi/\omega$. For a Newtonian fluid, this problem is analysed for example in White [16] and, with the normalization

$$T = \omega t; \quad Y = \frac{y}{h}; \quad U = u \frac{\omega}{K_O}; \quad \alpha = \frac{h}{\sqrt{\eta_0/\omega\rho}}; \quad (23)$$

$$T_{xy} = \tau_{xy} \frac{\omega h}{\eta_0 K_O} \quad (23)$$

where the time scale is now taken as the angular period and α is the Stokes or Womersley number, it is possible to obtain the solution:

$$U(Y, T) = \frac{\alpha^2 K_S}{2 K_O} (1 - Y^2) + Re \left\{ i \left[\frac{\cosh(\sqrt{i}\alpha Y)}{\cosh(\sqrt{i}\alpha)} - 1 \right] \exp(iT) \right\} \quad (24)$$

here written in terms of complex numbers. Alternatively, by using Moivre expression for the imaginary expressions, it is possible to write the solution under the following explicit form:

$$U(Y, T) = \frac{\alpha^2 K_S}{2 K_O} (1 - Y^2) + \left[1 - \frac{M(Y, \alpha')}{J(\alpha')} \right] \sin(T) - \frac{N(Y, \alpha') \cos(T)}{J(\alpha')} \quad (25)$$

where

$$\alpha' \equiv \alpha/\sqrt{2} = h/\sqrt{2\nu/\omega}$$

$$C(x) \equiv \cosh(x) \cos(x); \quad S(x) \equiv \sinh(x) \sin(x); \quad J(x) = C^2(x) + S^2(x)$$

$$M(Y, \alpha') = C(\alpha' Y)C(\alpha') + S(\alpha' Y)S(\alpha')$$

$$N(Y, \alpha') = C(\alpha' Y)S(\alpha') + S(\alpha' Y)C(\alpha')$$

Another relevant variable is the shear stress which can be obtained by differentiating Eq. (24) in order to Y :

$$T_{xy} = -\frac{\alpha'}{J(\alpha')} \left\{ [(A - B)C(\alpha') + (A + B)S(\alpha')] \sin(T) + [(A - B)S(\alpha') - (A + B)C(\alpha')] \cos(T) \right\} - \alpha'^2 \frac{K_S}{K_O} Y \quad (26)$$

where

$$A = \sinh(\alpha' Y) \cos(\alpha' Y)$$

$$B = \cosh(\alpha' Y) \sin(\alpha' Y) \quad (27)$$

The choice of values for the non-dimensional parameters were guided by the experiments of Khodadadi et al. [27], with a Reynolds number, based on the stationary mean streamwise velocity in the channel $\bar{u}_S = h^2 \rho K_S / 3 \eta_0$ and channel height $H = 2h$, of $Re = 102$, and a Stokes number of $\alpha = 4.864$. The oscillatory pressure gradient frequency, $\omega = 2\pi f$, was considered to be $f = 1.1$ cycles/s and its amplitude $\rho K_O = 190$ Pa/m; the stationary pressure gradient amplitude was $\rho K_S = 73.45$ Pa/m. Physical properties were fluid density $\rho = 1150$ kg/m³ and kinematic viscosity $\nu = 0.73 \times 10^{-5}$ m²/s. Of course, only the non-dimensional parameters, $\alpha = 4.864$ and $K_O/K_S = 2.587$ are of relevance, together with E and the Weissenberg number $Wi = 3.765$ introduced below for the viscoelastic case.

Pulsatile flow of an Oldroyd-B fluid in a channel subject to an oscillatory pressure gradient is a much more difficult problem which was tackled initially by Hayat et al. [28] who arrived at a solution only for the velocity profile. Here we take this problem a step further and derive the solution for the stress component profiles which are required for a complete assessment of the numerical predictions. The starting equation is again Eq. (16) but the imposed pressure gradient varies in time according to Eq. (22). Since Eq. (16) is linear, the resulting velocity will be given by the sum of solutions for the stationary and the oscillatory pressure gradients, $U = U_S(Y) + U_o(Y, T)$. The stationary part $U_S(Y)$ is equal to the steady state velocity profile for a Newtonian fluid subject to a constant pressure gradient ρK_S and is easily obtained as the 1st term on the right-hand side of Eq. (24). With the normalization introduced by Eq. (23), the oscillatory part of the velocity profile is the solution of:

$$\left[1 + \omega\lambda \frac{\partial}{\partial T} \right] \frac{\partial U_o}{\partial T} = \left[1 + \omega\lambda \frac{\partial}{\partial T} \right] \cos(T) + \frac{1}{\alpha^2} \left[1 + \omega\lambda_r \frac{\partial}{\partial T} \right] \frac{\partial^2 U_o}{\partial Y^2} \quad (28)$$

By assuming that velocity evolves in time with the same frequency of the pressure gradient but with some phase lag, the solution has the form:

$$U_o(Y, T) = Re [F(Y) \exp(iT)] \quad (29)$$

and upon substitution in Eq. (28) we arrive at the ordinary differential equation for $F(Y)$:

$$i(1 + i\omega\lambda)F = (1 + i\omega\lambda) + \frac{1}{\alpha^2}(1 + i\omega\lambda_r)F'' \quad (30)$$

The non-homogeneous ODE to be solved is then defined by:

$$iz_1 F = z_1 + \frac{z_2}{\alpha^2} F'' \quad (31)$$

with

$$z_1 = 1 + i\omega\lambda \quad \text{and} \quad z_2 = 1 + i\omega\lambda_r \quad (32)$$

subject to boundary conditions (no-slip at walls; symmetry at centreline):

$$\begin{aligned} F(1) = F(-1) &= 0 \\ F'(0) &= 0 \end{aligned} \quad (33)$$

By making the change of variables $G = F + i$ an homogeneous second order ODE is obtained:

$$G'' - i\alpha^2 \frac{z_1}{z_2} G = 0 \quad (34)$$

whose characteristic equations is:

$$\begin{aligned} z^2 - i\alpha^2 \frac{z_1}{z_2} = 0 &\Rightarrow z = \alpha \sqrt{i \frac{z_1}{z_2}} = \alpha \sqrt{i \frac{1 + i\omega\lambda}{1 + i\omega\lambda_r}} \Rightarrow z \\ &= \alpha \sqrt{i \frac{1 + i\alpha^2 E}{1 + i\beta\alpha^2 E}} \end{aligned} \quad (35)$$

where $E = \eta_0 \lambda / \rho h^2$ (Eq. (21)), and general solution

$$G = A \cosh(zY) + B \sinh(zY) \quad (36)$$

With the BCs $G(1) = G(-1) = i$ and $G'(0) = 0$ we obtain $A = i/\cosh z$ and $B = 0$, and the solution in terms of the oscillatory velocity profile becomes:

$$U_0(Y, T) = \text{Re} \left\{ i \left[\frac{\cosh(zY)}{\cosh(z)} - 1 \right] \exp(iT) \right\} \quad (37)$$

The channel velocity for the Oldroyd-B fluid with both stationary and oscillatory contributions to the pressure gradient is then:

$$U(Y, T) = \frac{\alpha^2 K_S}{2} (1 - Y^2) + \text{Re} \left\{ i \left[\frac{\cosh(zY)}{\cosh(z)} - 1 \right] \exp(iT) \right\} \quad (38)$$

In this case, unlike the Newtonian problem, stresses need to be derived from integration of the two constitutive equations, for τ_{xy} and τ_{xx} . Having obtained the velocity profile, we can go back to the momentum Eq. (3) and express it in terms of the elastic component of the shear stress:

$$\tau_{xy} = \rho \int_0^y \frac{\partial u}{\partial t} dy' - \rho(K_S + K_0 \cos \omega t)y - \eta_s \frac{\partial u}{\partial y} \quad (39)$$

with the spatial and time derivatives of $u(y,t)$ readily calculated from the dimensional form of the velocity solution, Eq. (38):

$$\frac{\partial u}{\partial y} = -\frac{h\rho K_S}{\eta_0} \left(\frac{y}{h} \right) + \frac{K_0}{\omega} \text{Re} \left\{ i \frac{z}{h} \left[\frac{\sinh(z(y/h))}{\cosh(z)} \right] \exp(i\omega t) \right\} \quad (40)$$

$$\frac{\partial u}{\partial t} = -K_0 \text{Re} \left\{ \left[\frac{\cosh(z(y/h))}{\cosh(z)} - 1 \right] \exp(i\omega t) \right\} \quad (41)$$

Upon substitution of Eqs. (40) and (41) into Eq. (39), and after regrouping the various terms, we arrive at the dimensional expression for the elastic shear stress:

$$\tau_{xy} = -\rho h K_S (1 - \beta) \frac{y}{h} - \rho h K_0 \text{Re} \left\{ \exp(i\omega t) \frac{\sinh(zY/h)}{\cosh(z)} \left[\frac{1}{z} + \frac{i\beta z}{\alpha^2} \right] \right\} \quad (42)$$

For the quasi-linear Oldroyd-B model the axial normal stress does not influence the fluid motion but its analytical expression will be useful to assess the numerical method. Under the present

simplifying assumptions, Eq. (4) for the normal component reduces to:

$$\tau_{xx} + \lambda \frac{\partial \tau_{xx}}{\partial t} = 2\lambda \tau_{xy} \frac{\partial u}{\partial y} \quad (43)$$

which has the general solution:

$$\tau_{xx} = \exp\left(\frac{-t}{\lambda}\right) \int_{-\infty}^t 2\tau_{xy} \frac{\partial u}{\partial y} \exp\left(\frac{t'}{\lambda}\right) dt' \quad (44)$$

Now, with τ_{xy} from Eq. (42) and $\partial u/\partial y$ from Eq. (40), the integral in Eq. (44) can be performed and, after a lengthy derivation which is here omitted for the sake of conciseness, we arrive at the following result for the normal stresses in dimensional form:

$$\begin{aligned} \tau_{xx} &= \frac{2\lambda}{\eta_0} (\rho h K_S)^2 (1 - \beta) \frac{y^2}{h} - 2 \left(\frac{K_0}{K_S} \right) \frac{\lambda (\rho h K_S)^2 y}{\rho h^2 \omega} \text{Re} \\ &\times \left\{ \frac{\exp(i\omega t)}{1 + i\omega\lambda} \frac{\sinh(zY/h)}{\cosh(z)} \left[iz(1 - 2\beta) - \frac{\alpha^2}{z} \right] \right\} \\ &- 2 \left(\frac{K_0}{K_S} \right)^2 \frac{\lambda (\rho h K_S)^2}{\rho h^2 \omega} \text{Re} \left\{ \frac{\exp(i2\omega t)}{1 + i2\omega\lambda} \left(\frac{\sinh(zY/h)}{\cosh(z)} \right)^2 \right. \\ &\times \left. \left[i - \frac{\beta z^2}{\alpha^2} \right] \right\} \end{aligned} \quad (45)$$

Under non-dimensional form, with standard scaling based on the average channel velocity for the steady pressure gradient ρK_S and wall shear stress in channel flow $\tau_w = 3\eta_0 \bar{u}_s/h$ the solution is written as:

$$\begin{aligned} U(Y, T) &\equiv \frac{u}{\bar{u}_s} = \frac{3}{2} (1 - Y^2) + \frac{3K_0}{\alpha^2 K_S} \text{Re} \\ &\times \left\{ i \left[\frac{\cosh(zY)}{\cosh(z)} - 1 \right] \exp(2\pi i T) \right\} \end{aligned} \quad (46)$$

$$\begin{aligned} T_{xy}(Y, T) &\equiv \frac{\tau_{xy}}{\tau_w} = -(1 - \beta)Y - \frac{K_0}{K_S} \text{Re} \\ &\times \left\{ \exp(2\pi i T) \frac{\sinh(zY)}{\cosh(z)} \left[\frac{1}{z} + \frac{i\beta z}{\alpha^2} \right] \right\} \end{aligned} \quad (47)$$

$$\begin{aligned} T_{xx}(Y, T) &\equiv \frac{\tau_{xx}}{\tau_w} = 6Wi(1 - \beta)Y^2 - 6 \left(\frac{K_0}{K_S} \right) \frac{Wi}{\alpha^2} Y \text{Re} \\ &\times \left\{ \frac{\exp(2\pi i T)}{1 + i\alpha^2 E} \frac{\sinh(zY)}{\cosh(z)} \left[iz(1 - 2\beta) - \frac{\alpha^2}{z} \right] \right\} \\ &- 6 \left(\frac{K_0}{K_S} \right)^2 \frac{Wi}{\alpha^2} \text{Re} \left\{ \frac{\exp(4\pi i T)}{1 + i2\alpha^2 E} \left(\frac{\sinh(zY)}{\cosh(z)} \right)^2 \right. \\ &\times \left. \left[i - \frac{\beta z^2}{\alpha^2} \right] \right\} \end{aligned} \quad (48)$$

Here time is scaled with the period of the oscillation $T \equiv t/T_0$, instead of the angular frequency as in Eq. (23); the results to be presented in the next section are compared with the analytical solution given by Eqs. (46)–(48). It is interesting to notice that while U and T_{xy} depend only on α , K_0/K_S , β and E , the normal stress component T_{xx} also depends on Wi , reflecting the influence of elasticity through the first-normal stress difference.

These analytical solutions will be helpful to compute exactly the discretization error of the numerical predictions. To do this, an error

measure based on the Euclidian norm was calculated for the axial velocity $U(T,Y)$ as:

$$e(T) = \sqrt{\frac{1}{NY} \sum_i (U_{\Delta y}(Y_i, T) - U(Y_i, T))^2} \quad (49)$$

where U is the analytical solution and $U_{\Delta y}$ the numerical solution on a mesh with NY control volumes and mesh spacing $\Delta y = h/NY$. Note that the error calculated in this way is a global value evaluated by integration over the channel cross-section but varies with time T . It is also possible to measure the error based on a local velocity value, for example by taking the centreline velocity and comparing the predicted value against the theoretical result, $e(U_0) = |U_{\Delta y}(0, T) - U(0, T)|$, as in Ref. [5], but we found this procedure to yield a less smooth error variation.

5. Numerical results and discussion

In this section the results obtained with the numerical method outlined in Section 3, applied to the two benchmark flow problems described in Section 4, are presented and discussed. First, the study of start-up planar Poiseuille flow of a Newtonian fluid is shortly addressed (Section 5.1) and then the UCM model is considered in more detail, with results discussed in terms of the accuracy achieved with respect to mesh and time step refinement (Section 5.2). The analysis is extended to Oldroyd-B, PTT and FENE-CR models, where the optimal mesh size and time step previously determined are employed, and velocity profiles corresponding to several specific moments in time are shown and discussed (Section 5.3). An analogous study is presented for the pulsating flow test case where results for the Newtonian (Section 5.4), UCM and Oldroyd-B (Section 5.5) fluids are shown and a comparison between theoretical and numerical results was possible. In these two subsections the non-dimensional frequency, measured by the Womersley number, and the pressure-gradient ratio were fixed at the values $\alpha = 4.864$ and $K_0/K_S = 2.587$, respectively.

5.1. Start-up planar Poiseuille flow of a Newtonian fluid

As a preliminary check, the program was first used for the simulation of a Newtonian fluid. Several consistently refined meshes were employed with $NY = 20, 40, 80, 160, \dots$, uniform control volumes along the y direction, corresponding to normalized mesh spacings of $\Delta y = 0.05, 0.025, 0.0125, \dots$.

Fig. 2 shows the evolution of centreline velocity during the start-up of planar Poiseuille flow of a Newtonian fluid predicted on mesh $NY = 80$. As can be seen, the numerical results fit very well the analytical curve of Eq. (14). In this case the time step used was $\Delta t = 0.0125$ in terms of the diffusive time scale of Eq. (13), a rather small value. With larger time steps the numerical results were still very accurate and no differences could be perceived in a graph. This is due to the good accuracy of the second-order temporal scheme here utilized based on a three time level discretization scheme for the time derivative, Eq. (10). The inset in Fig. 2 shows the convergence rates for the three-time level (3TL) and the implicit Euler methods in terms of the absolute norm of the error of the centreline velocity at time $T = 0.5$ during the transient process. Symbols are the actual results and the lines are power-law best fits provided by the graph program. Rates of convergence of 0.98 and 2.04 are found for the formally 1st and 2nd order Euler and 3TL methods. Another important point demonstrated by the inset in Fig. 2 is that the 3TL method requires careful attention to the first time step and the initial conditions to the method. When care is not exercised, as shown by the cross symbols in the inset, the convergence rate is only $p = 1.03$ typical of a 1st order method. To achieve 2nd order,

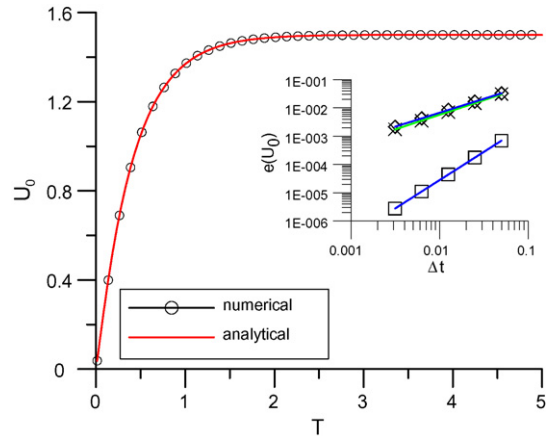


Fig. 2. Evolution of centreline velocity with time during the start-up of a Newtonian fluid ($\Delta t = \Delta y = 1.25 \times 10^{-2}$). Inset: convergence rate for 3 schemes: three-time level (squares), same without using Euler for initial step (crosses), and implicit Euler (diamonds).

we employed in all calculations the Euler method for the first time step when starting from a quiescent field.

Fig. 3 shows analytical and numerical velocity profiles at different instants in time of the transient process leading eventually to the steady state parabolic profile. This state occurs when the time, normalized by a diffusion time scale, is greater than approximately $T \geq 3-4$. Only half of the profiles are shown because the calculations were made using half of the geometry by assuming symmetry at $y = 0$. Again, it can be seen that the program mimics very well the theoretical response.

5.2. Start-up planar Poiseuille flow of an UCM fluid

First we look at the spatial discretization error, which was determined using five computational meshes with 50 (MESH 1), 100 (MESH 2), 200 (MESH 3), 400 (MESH 4) and 800 (MESH 5) uniform CV for the discretization of the flow domain along the y direction. We ran several numerical calculations using these five meshes at an elasticity number of $E = 1$. For this case, the numerical results for the centreline velocity ($y = 0$) using MESH 2 and a small time step equal to 1.25×10^{-3} are shown in Fig. 4 where are compared with the analytical profile Eq. (17). Clearly, hardly any difference is seen

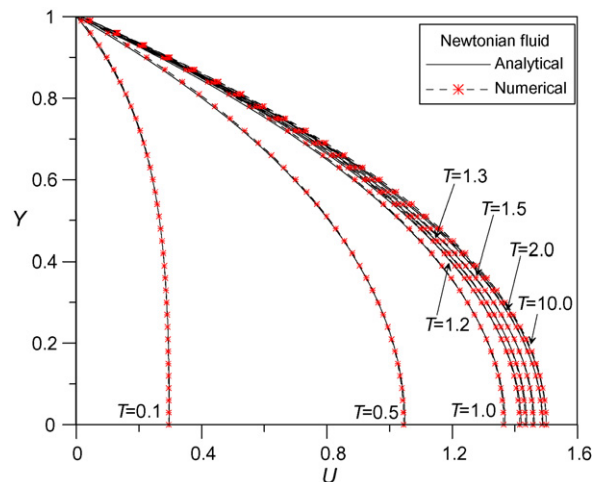


Fig. 3. Velocity profiles of a Newtonian fluid at different non-dimensional times ($\Delta t = 1 \times 10^{-3}$ and $\Delta y = 1 \times 10^{-2}$).

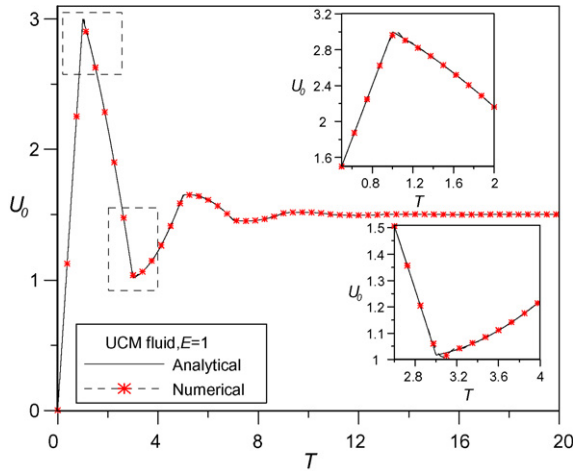


Fig. 4. Evolution of centreline velocity with time during the start-up of an UCM fluid at $E=1$ ($\Delta t=1.25 \times 10^{-3}$ and $\Delta y=1 \times 10^{-2}$).

in this figure, indicating an accurate solution and that this mesh is perfectly adequate to resolve the velocity variation.

The discretization error was calculated along the simulations by using Eq. (49) and the results on the first 3 meshes are given in Fig. 5 for decreasing values of Δy and a fixed $\Delta t=1.25 \times 10^{-3}$. It can be seen that the error diminishes with mesh refinement, as would be anticipated, and it is small for all meshes—typically around order 10^{-3} on the finest mesh. A qualitative estimate of the order of convergence can be done by considering errors at a given time; for example, at $T=1.5$ the errors on the 3 meshes are 7.81, 3.95 and $2.04 (\times 10^{-3})$, indicating an error reduction of about 2 as the mesh is doubled.

A similar study of the effect of time step refinement on the error evolution for a fixed mesh (MESH 2), starting with $\Delta t=0.01$ and halving it until a value of $\Delta t=1.25 \times 10^{-3}$ is reached, also showed that the error decay scales approximately with Δt and tends to saturate as the time step gets smaller. An explanation for such lack of 2nd, and even 1st, order behaviour when Δt is refined may reside on two points: first, the spatial discretization is controlling the error, having a stronger influence when compared to time step refinement, and therefore one should use much finer meshes to study in detail the temporal error decay; and second, the discontinuities in

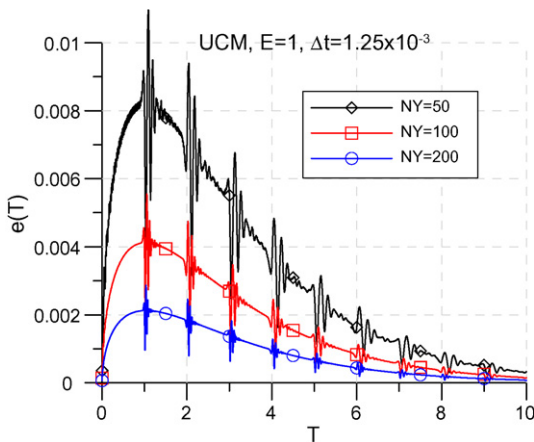


Fig. 5. Influence of mesh refinement on the evolution of the discretization error during the start-up of an UCM fluid at $E=1$ ($\Delta t=1.25 \times 10^{-3}$; MESH 1 with $\Delta y=0.02$; MESH 2 with $\Delta y=0.01$; MESH 3 with $\Delta y=0.005$).

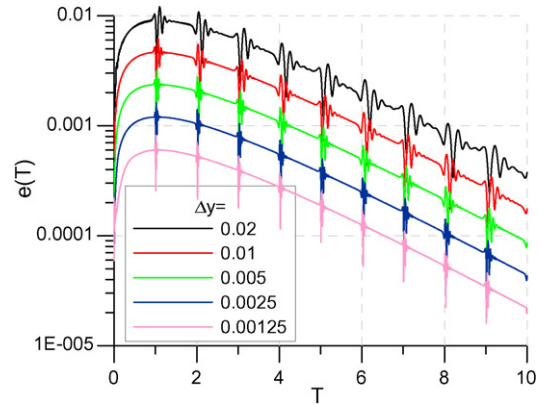


Fig. 6. Influence of consistent mesh and time step refinement on the evolution of the discretization error during the start-up of an UCM fluid at $E=1$ ($\Delta t=0.5\Delta y$).

the solution, to be further commented below, are such that error accumulation decreases the rate of convergence to only 1st order in time.

Regarding the first of these points, it is possible to devise a better refinement procedure which overcomes that limitation. Since the method is formally 2nd order in space and time, the error should scale as $e=A\Delta t^2+B\Delta y^2$, and by using a proportional space and time refinement, $\Delta t=C\Delta y$, we should end up with a global 2nd order behaviour,

$$e = (AC^2 + B)\Delta y^2 = Cte \times \Delta y^2 \equiv Cte \times \Delta y^p \quad (50)$$

where p is the order of convergence of the method. With the meshes mentioned above, and with a corresponding series of progressively smaller time steps (for the UCM we used $\Delta t=0.5\Delta y$, that is $C=0.5$) then the computed errors evolution are shown in Fig. 6. Under this representation there is a clear convergence with simultaneous Δy and Δt refinement, with uniform separation of the error decay curves (ideally should be $2\log_2$ for a 2nd order scheme). A convergence plot of errors evaluated using $\Delta y=(1/C)\Delta t=C'\Delta t$ ($C'=1$ for $\beta \geq 0.1$ and $C'=2$ for $\beta \leq 0.1$) is shown in Fig. 7 for Oldroyd-B fluids in a range of β and the UCM ($\beta=0$) for both the three-time level and the Euler methods, with the lines corresponding to power-law best fits. For the Oldroyd-B fluids the convergence rate is $p=2.00$ for all β cases on the 3 most refined meshes (decreasing to $p=1.83$ for $\beta=0.001$ when all 5 discretizations are considered); for the UCM the rate is 0.99 for the 3TL and 0.78 for the implicit Euler scheme which also exhibits errors higher by about a factor of 3. And worst, the dissipative nature of the Euler scheme leads to very

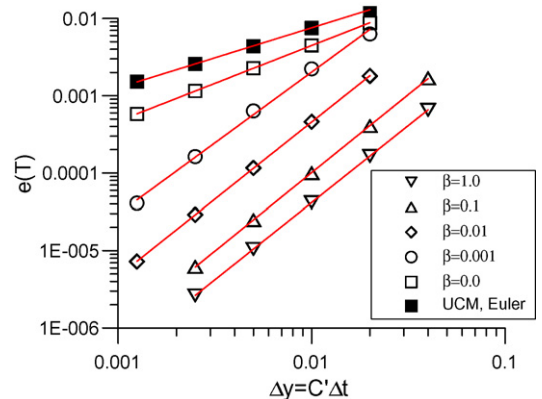


Fig. 7. Convergence rates for the start-up of UCM ($\beta=0$) and Oldroyd-B ($\beta=0.1-0.001$) fluids at $E=1$ ($\Delta y=\Delta t$ for $\beta > 0.1$; $\Delta y=2.0\Delta t$ for $\beta \leq 0.1$).

strong damping of the periodic and localised error oscillations seen in Fig. 6, separated by time delays of 1 unit. These features correspond to shear wave propagation to be discussed in more detail in the next paragraphs. Based on the results of Figs. 5 and 6, it was decided to use *MESH 2* and $\Delta t = 1.25 \times 10^{-3}$ on most other simulations of the start-up flow as they give adequate results within a reasonable time frame. It is also relevant to point out at this stage that 2nd order accuracy could be obtained due to the use of the new method of implementing wall boundary conditions, Eq. (12); with the previous method, Eq. (11) the order of convergence would be reduced to $p = 1.11$ with Oldroyd-B $\beta = 0.01$, and $p = 1.01$ with $\beta = 0.1$.

Additionally, a number of points already discussed can be observed in those figures. Errors are magnified periodically, with a non-dimensional period of unity, on account of discontinuities in the time derivative of the velocity field. These discontinuities are recognized as a front of shear waves propagating from the wall towards the centreline with a certain propagation speed c . This speed can be evaluated from a simplified analysis, starting with the momentum equation (Eq. (3), without solvent viscosity) and the UCM equation (Eq. (4) with $f = f = 1$ and $\eta_0 = \eta_p$) for the shear stress component ($\tau \equiv \tau_{xy}$) here re-written as:

$$\rho \frac{\partial u}{\partial t} = -\frac{dp}{dx} + \frac{\partial \tau}{\partial y} \quad \text{and} \quad \tau + \lambda \frac{\partial \tau}{\partial t} = \eta_0 \frac{\partial u}{\partial y}$$

In order to transform these two equations into a typical hyperbolic equation having the form $\partial^2 \phi / \partial t^2 = c^2 \partial^2 \phi / \partial y^2$, where c is the wave speed (e.g. the equation for a vibrating string), the first is differentiated with respect to space and the second with respect to time, giving:

$$\rho \frac{\partial}{\partial t} \frac{\partial u}{\partial y} = \frac{\partial^2 \tau}{\partial y^2} \quad \text{and} \quad \frac{\partial \tau}{\partial t} + \lambda \frac{\partial^2 \tau}{\partial t^2} = \eta_0 \frac{\partial}{\partial t} \frac{\partial u}{\partial y}$$

Substituting the first of this latter set into the second of them, gives:

$$\frac{\partial^2 \tau}{\partial t^2} + \frac{1}{\lambda} \frac{\partial \tau}{\partial t} = \frac{\eta_0}{\lambda \rho} \frac{\partial^2 \tau}{\partial y^2}$$

and comparing with the above typical hyperbolic equation we recognise a similar equation, possessing an additional attenuation term and implying a dimensional shear-stress wave speed of $c^2 = \eta_0 / \lambda \rho$. In non-dimensional terms, which is more useful to compare with our start-up flow results, we set $\tau^* = \tau / \tau_w$, $T = t / \lambda$, $Y = y / h$, $E = \eta_0 / \lambda \rho h^2$ (as in Eq. (21)), and the damped hyperbolic equation becomes:

$$\frac{\partial^2 \tau^*}{\partial T^2} + \frac{\partial \tau^*}{\partial T} = E \frac{\partial^2 \tau^*}{\partial Y^2} \quad (51)$$

showing that the non-dimensional speed for propagation of stress waves is:

$$c = \sqrt{E} \quad (52)$$

The non-dimensional period, on the other side, is obtained by considering that space equals time multiplied by velocity, which for a non-dimensional space of unity (dimensionally, it is h) gives:

$$T_c = \frac{1}{\sqrt{E}} \quad (53)$$

For the present case of $E = 1$, leading to a (non-dimensional) propagation velocity of $c = 1$ according to Eq. (52), and so oscillations should appear separated by time intervals of unity, as confirmed by the first peak in Fig. 4. Although all these discontinuities are too subtle to be observed in Fig. 4 for larger times, they do exist and are magnified in the error plots of Figs. 5 and 6. The oscillatory response of velocity to the instantaneously applied

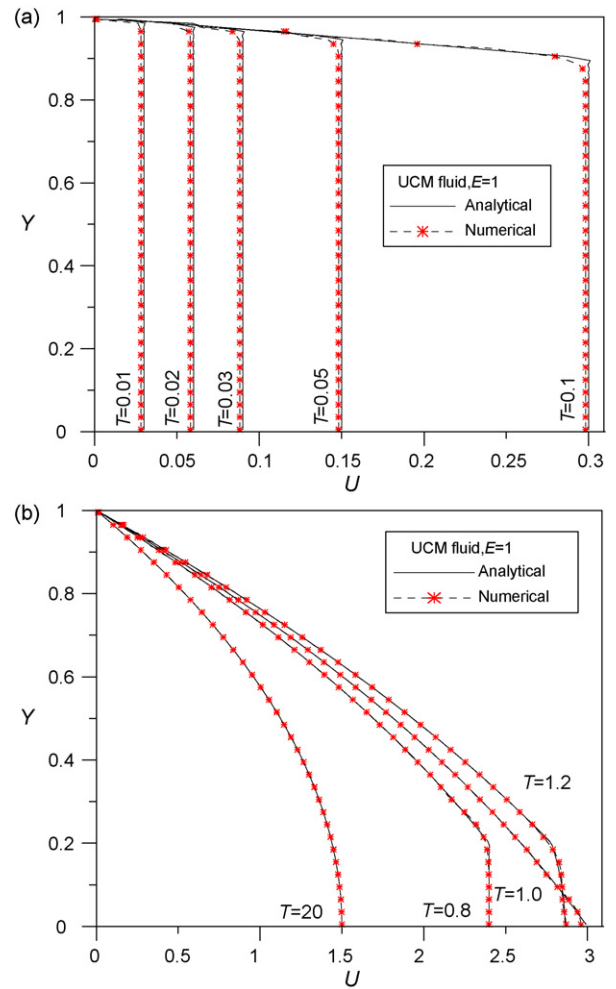


Fig. 8. Velocity profiles of an UCM fluid at different non-dimensional times at $E = 1$ ($\Delta t = 1.25 \times 10^{-3}$ and $\Delta y = 1 \times 10^{-2}$): (a) $T = 0.01-0.1$; (b) $T = 0.8-20.0$.

pressure gradient is better seen by using larger elasticity numbers. It was confirmed that with $E = 2$ error peaks appear separated by a period of $1/\sqrt{2} = 0.7$, and with $E = 4$ the period is 0.5. From the zoomed insets in Fig. 4(b) and (c) the differences between numerical and analytical responses become more discernible. The discontinuities of the analytical solution for the temporal velocity profile at $y = 0$ lead to numerical oscillations. As a consequence, the numerical and analytical results agree very well except in the vicinity of these peaks, where small oscillations and damping motions can be observed in the numerical solution. We also noticed that the frequency of the small oscillations from numerical origin is accentuated when the time step becomes smaller, but globally the answer is closer to the analytical solution given by Waters and King [17].

We turn attention now to the local velocity variation at $E = 1$ with the UCM model. Fig. 8(a) and (b) present velocity profiles on *MESH 2* at different time moments and provide a comparison between numerical results and analytical solution. These profiles were obtained at times shortly after start-up ($T = 0.01-0.1$), during the first peak ($T = 0.8-1.2$) and when the flow had reached steady state ($T = 20$). With this model and for the earlier times, shortly after start-up, some differences are perceived but in relative terms they are small. It can be observed that the velocity gradient in the analytical solutions has discontinuities which are hard to resolve numerically without resorting to local mesh refinement. These discontinuities correspond to shear wave front positions, as discussed

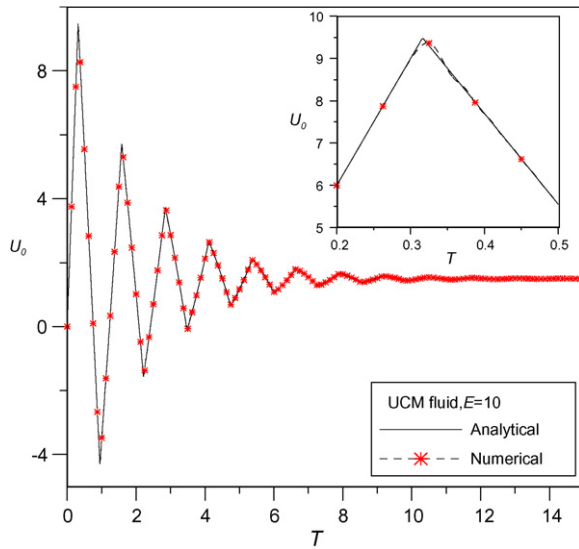


Fig. 9. Evolution of centreline velocity with time during the start-up of an UCM fluid at $E = 10$ ($\Delta t = 1.25 \times 10^{-4}$ and $\Delta y = 1 \times 10^{-2}$).

above; a shear wave starts from the upper wall at $T = 0$, propagates towards the centreline, is reflected on the other wall, propagates back to the first wall, and so on. This shear wave causes the low-frequency oscillatory movement previously seen in Fig. 4.

Next we analyse the centreline velocity evolution obtained during the start-up planar Poiseuille flow of the UCM fluid at higher values of the elasticity number, namely for $E = 10$ and 100 , compared with the previous value of $E = 1$. For both cases we used *MESH 2* but smaller time-steps than with $E = 1$, because of the expected higher frequency of the response. Fig. 9 shows the evolution of centreline velocity at $E = 10$ using $\Delta t = 1.25 \times 10^{-4}$ and Fig. 10 shows the evolution of the centreline velocity at $E = 100$ using a time step of 2.5×10^{-5} . In each figure there is a local plot zooming into the first peak so that the numerical oscillations already discussed for $E = 1$ are better seen. As a consequence of increased elasticity, much higher oscillatory frequencies and amplitudes are observed in the transient process: Eq. (53) predicts periods of $1/\sqrt{10}$ and $1/\sqrt{100}$ separating the velocity peaks in Figs. 9 and 10, respectively;

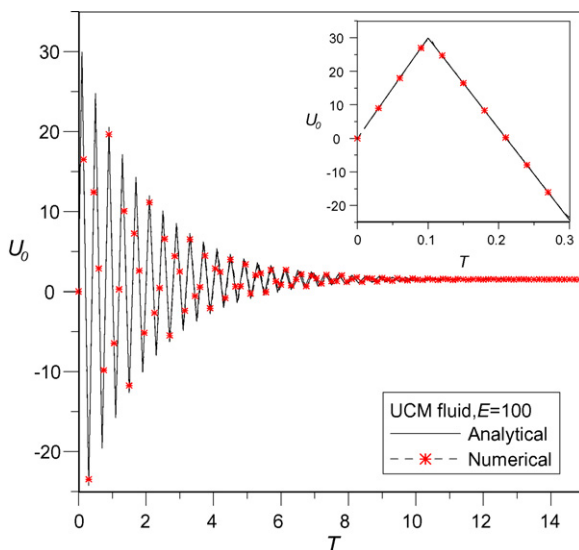


Fig. 10. Evolution of centreline velocity with time during the start-up of planar Poiseuille flow of an UCM fluid at $E = 100$ ($\Delta t = 2.5 \times 10^{-5}$ and $\Delta y = 1 \times 10^{-2}$).

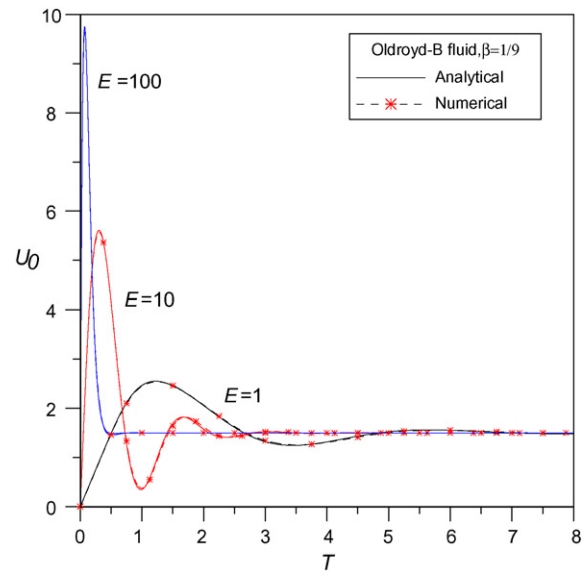


Fig. 11. Evolution of centreline velocity with time during the start-up of an Oldroyd-B fluid ($\beta = 1/9$) on mesh $\Delta y = 1 \times 10^{-2}$ at three elasticity numbers: $E = 1$ ($\Delta t = 1.25 \times 10^{-3}$); $E = 10$ ($\Delta t = 1.25 \times 10^{-4}$); $E = 100$ ($\Delta t = 2.5 \times 10^{-5}$).

these predictions are exactly confirmed by the numerical results. The analytical solution is once more fairly well reproduced by the numerical predictions, even if the error in frequency gets larger as time proceeds, tending to accumulate and eventually leading to an erroneous response in frequency (cf. phase lag in Fig. 10, $E = 100$, for large times). This error in frequency can be reduced by using smaller steps in time.

5.3. Start-up planar Poiseuille flow of Oldroyd-B, PTT and FENE-CR fluids

Results for start-up Poiseuille flow of Oldroyd-B, PTT and FENE-CR fluids are now presented. In these calculations we shall use the most cost-effective mesh and time step, as determined from the previous section. We begin with the Oldroyd-B flow which has an analytical solution [17]. For this model it was already shown (Fig. 7) that the method converges in a second order manner ($p = 2.00$ for $\beta = 1.0, 0.1$ and 0.001 ; $p = 1.98$ for $\beta = 0.001$ on the 3 more refined discretizations; on all 5 discretizations, $p = 1.99$ for $\beta = 1.0$ and 0.01 , $p = 2.02$ for $\beta = 0.1$, and $p = 1.83$ $\beta = 0.001$). Fig. 11 presents the temporal variation of centreline velocity at $E = 1, 10$ and 100 for $\beta = 1/9$, a commonly used value; for the start-up flow, it was adopted by Webster et al. [8], Fietier and Deville [9] and Van Os and Phillips [10], while Xue et al. [5] applied $\beta = 0.4$ and 0 . Agreement between analytical and numerical solutions is very good, showing that accuracy is much better when some solvent viscosity is present. The steady state, indicated by $U_0 = 1.5$, is reached much faster now than for the UCM model, and the transient is also seen to be shorter (in relaxation time units) for the larger elasticity cases.

Velocity profiles for the Oldroyd-B fluid with $E = 1$ are shown in Fig. 12 where it is plain to notice that they are markedly different from those obtained with the UCM model (Fig. 8). Unlike this latter fluid, the linear momentum conservation equation for the Oldroyd-B fluid includes a term equivalent to a Newtonian viscosity. Hence, the diffusion speed is infinite inhibiting the formation of a shear wave and the gradient discontinuities observed in the previous section are smeared out in Figs. 11 and 12. These show a smooth development of the transient centreline velocity evolution and of the spatial variation of the flow field, which is a consequence of the introduction of some physical diffusion in the equation of motion

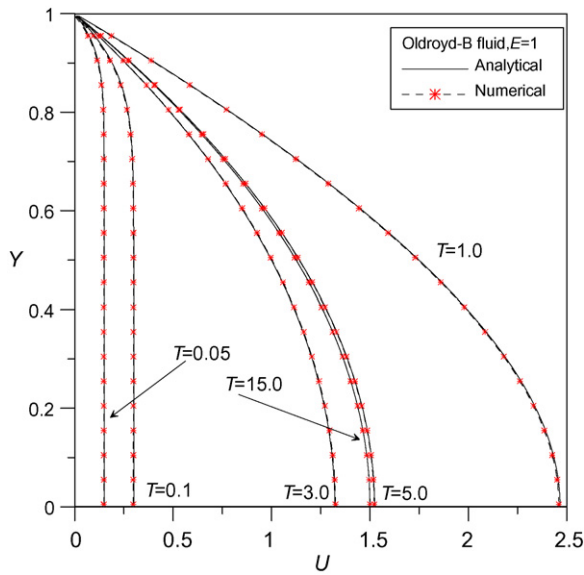


Fig. 12. Velocity profiles of an Oldroyd-B fluid ($\beta=1/9$) for $E=1$ at different non-dimensional times ($\Delta t=1.25 \times 10^{-3}$ and $\Delta y=1 \times 10^{-2}$).

by means of the finite solvent viscosity. Notice how the numerical results are now free of numerically induced oscillations and extraneous peak attenuation.

Next we look at the start-up planar Poiseuille flow of a PTT fluid without solvent viscosity and contrast it with the results already discussed. Fig. 13 shows the numerical results for the evolution of the centreline velocity of a PTT fluid with $E=1, 10$ and 100 . Since the PTT fluid with $\beta=0$ is a purely elastic fluid (devoid of “solvent viscosity”), the behaviour displayed in Fig. 13 is similar to that found for the UCM fluid in what concerns the velocity response after start-up, evidencing the moments the front of the shear wave reaches the centreline and is then successively reflected on the channel walls. A damped travelling wave and sharp localised oscillations are features that can be observed, much like the UCM cases in Figs. 4, 9 and 10. However, due to the shear-thinning property inherent to the PTT model, the steady state is accomplished earlier. Once

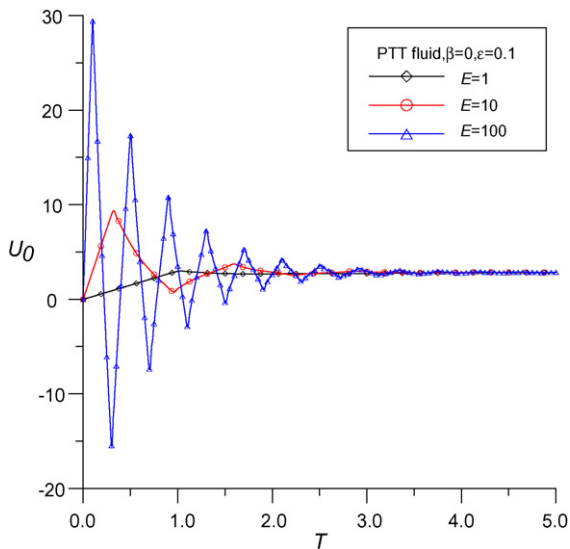


Fig. 13. Evolution of centreline velocity with time during the start-up of a PTT fluid ($\beta=0$ and $\epsilon=0.1$) on mesh $\Delta y=1 \times 10^{-2}$, at $E=1$ ($\Delta t=1.25 \times 10^{-3}$), $E=10$ ($\Delta t=1.25 \times 10^{-4}$) and $E=100$ ($\Delta t=2.5 \times 10^{-5}$).

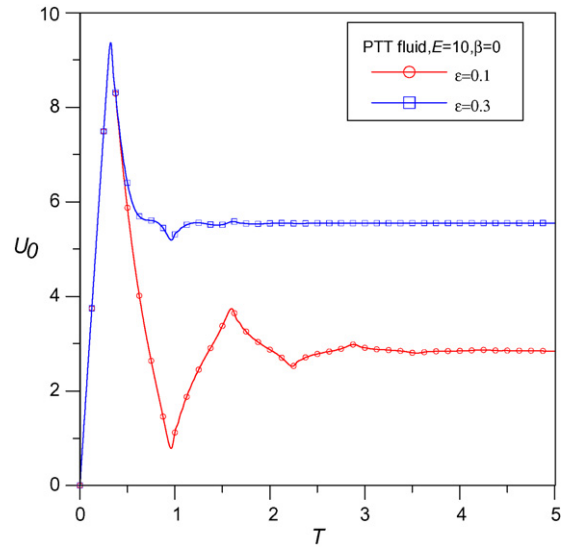


Fig. 14. Evolution of centreline velocity with time during the start-up of a PTT fluid ($\beta=0$) at $E=10$ ($\Delta t=1.25 \times 10^{-4}$ and $\Delta y=1 \times 10^{-2}$), for $\epsilon=0.1$ and $\epsilon=0.3$.

the front of the shear wave reaches the opposite wall after start-up, the degree of damping following successive reflections, seen by local maxima of U_0 , is significantly reduced compared to the UCM model (cf. [5]).

The effect of the extensibility parameter in the PTT model was also studied. At $E=10$ we obtained the temporal profiles shown in Fig. 14 with two different values of ϵ (0.1 and 0.3). Clearly, the velocity magnitude during start-up depends on ϵ as could be expected on account of shear-thinning in viscosity: for the same applied pressure-gradient, the average (and maximum, at centreline) velocity is larger for the PTT fluid with larger ϵ . It is observed that as the ϵ value grows, and the maximum plateau levels of extensional viscosity are greatly reduced, the PTT model yields results that are further away from those of the UCM model, and a smoother behaviour is achieved. For a smaller value of ϵ the oscillations become more accentuated, but the frequency of those oscillations, however faint, seems to be independent of ϵ .

Finally, Fig. 15 presents results obtained from numerical calculations of start-up planar Poiseuille flow for a FENE-CR fluid. In this case, we compare the centreline velocity profiles obtained with elasticity numbers of $E=1, 10$ and 100 , and extensibility parameter $L^2=100$ which is a common value used in benchmark problems when the purpose is to study the influence of extensibility, and a β value equal to 0.5, implying the same proportion of solvent and polymer viscosities. Fig. 15 shows that with such a model fluid the equivalent to the “shocks” of the UCM fluid are not generated and consequently numerical oscillations are absent, so that a smooth development of the velocity is patent in the figure. These results resemble those obtained with the Oldroyd-B model and are essentially a consequence of the solvent viscosity contribution. At $E=10$, results were also obtained for a smaller value of $L^2=10$. These are shown in Fig. 15 by the dashed line and the evolution of the centreline velocity follows a somewhat different path compared with the case $L^2=100$, which can be interpreted as the dumbbell having smaller extensibility tending to be fully stretched faster, followed by recovery and some tendency to a slightly oscillating pattern.

5.4. Pulsating planar flow of a Newtonian fluid

This subsection deals with code verification using Newtonian fluid test cases. Before considering the pulsating flow test case,

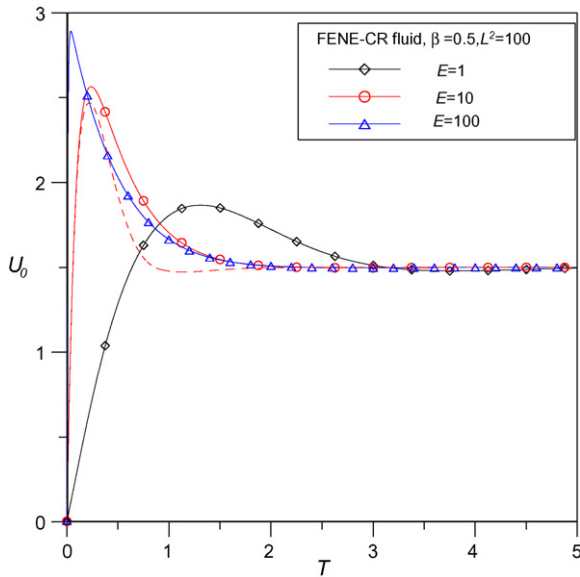


Fig. 15. Evolution of centreline velocity with time during the start-up of a FENE-CR fluid ($\beta=0.5, L^2=100$) on mesh $\Delta y=1 \times 10^{-2}$, at $E=1$ ($\Delta t=1.25 \times 10^{-3}$), $E=10$ ($\Delta t=1.25 \times 10^{-4}$) and $E=100$ ($\Delta t=2.5 \times 10^{-5}$). Dashed line: $E=10, L^2=10$.

preliminary steady calculations showed that numerical results for velocity and shear stress profiles in channel flow generated by the imposition of a stationary pressure gradient (that is, planar Poiseuille flow) presented a very good level of accuracy on the uniform 100 CV mesh (*MESH 2*). These results are useful as initial conditions for the pulsating regime. Then, after adding the oscillatory part to the stationary pressure gradient, transient numerical simulations were carried out for a number of periods using the three-time level method on the same *MESH 2* and a time-step of 1×10^{-2} (time is normalized with the oscillatory period, $2\pi/\omega$). It was important to carefully verify in these calculations that a fully established oscillatory regime was achieved, with repetition at every cycle.

Fig. 16 shows a comparison of analytical (lines) and numerical (symbols) velocity profiles at several moments in time during one cycle (at phase angles separated by 90°) with $\alpha=4.864$ and $K_0/K_S=2.587$ (to be used throughout this and the next subsections). It is observed that during the whole cycle there is a very good agreement between results, leading to the conclusion that the time step

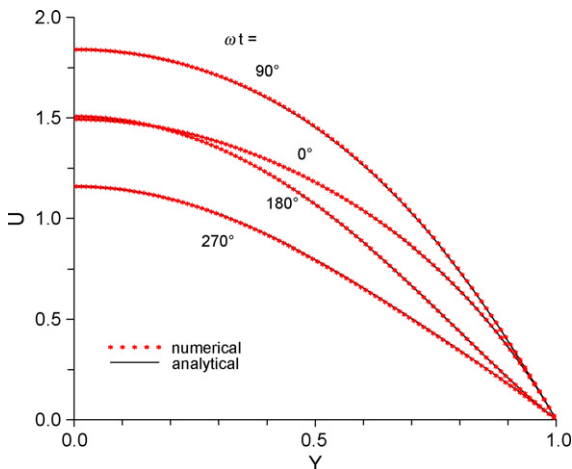


Fig. 16. Velocity profiles of a Newtonian fluid in the oscillatory regime during one cycle ($\Delta t=1 \times 10^{-2}$ and $\Delta y=1 \times 10^{-2}$).

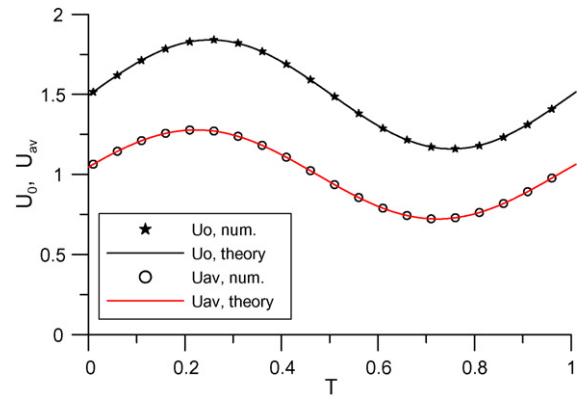


Fig. 17. Evolution of centreline (U_0) and average (U_{av}) velocities with time during the pulsating planar flow of a Newtonian fluid ($\Delta t=1 \times 10^{-2}$ and $\Delta y=1 \times 10^{-2}$).

1×10^{-2} is sufficient to accurately resolve the theoretical solution for the Newtonian fluid. From a convergence rate study, using both mesh and time step refinement according to Eq. (50) ($\Delta t = \Delta y$), the rate was found to be $p=2.00$ based on error Eq. (49), thus in agreement with second order behaviour.

Since the pressure gradient varies as a $\cos(\omega t)$, during one cycle there is a minimum of dp/dx at $\omega t=180^\circ$, a maximum at $\omega t=360^\circ$, and zeros at $\omega t=90^\circ$ and 270° ; we verify from Fig. 17, showing the centreline and cross-sectional average channel velocities, that the velocity variation has a phase difference when compared with pressure. Looking at the maximum velocity at the channel centreline, there is a phase difference of approximately 90° when compared with the pressure gradient. The evolution of the maximum velocity ($U_0 = u(y=0, t)/\bar{u}_S$) and of the average cross-sectional velocity in the channel ($U_{av} = \bar{u}(t)/\bar{u}_S = \int_0^h u(y, t) dy/h\bar{u}_S$) evolves with time as shown in Fig. 17 where a perfect match between numerical and analytical results is evident.

Another variable of interest in many applications is the shear stress. The evolution of this variable during one cycle is presented in Fig. 18 where a comparison between the numerical and theoretical (Eq. (26) with rescaling of τ_{xy} and t) results is made. Again, a very good agreement between numerical results and the analytical solution is observed as it was the case for the velocity profiles; the wall shear stress attains a maximum (in absolute terms) at 0° and 90° .

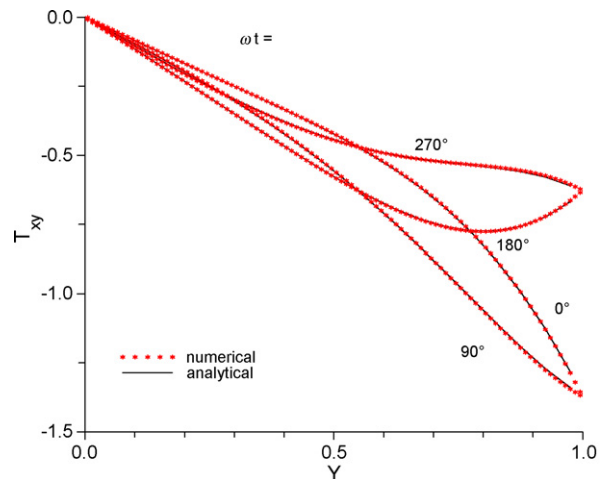


Fig. 18. Shear stress profiles of a Newtonian fluid in the oscillatory regime during one cycle ($\Delta t=1 \times 10^{-2}$ and $\Delta y=1 \times 10^{-2}$).

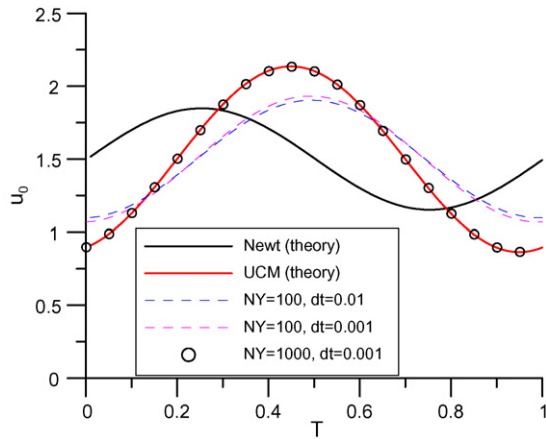


Fig. 19. Evolution of centreline velocity during one cycle for the pulsating flow of a Newtonian and an UCM ($E = 1$) fluid: influence of mesh and time-step refinement on predictions ($\Delta t = 10^{-2}$ to 10^{-3} and $\Delta y = 10^{-2}$ to 10^{-3}).

5.5. Pulsating planar flow of a non-Newtonian fluid

We consider now the more interesting situation of a viscoelastic fluid model subject to an oscillatory pressure gradient, in which we shall specifically employ either the UCM or the Oldroyd-B fluids, whose theoretical solution was derived in Section 4.2.

By comparing the evolution of the centreline velocity during one cycle for a Newtonian fluid and a viscoelastic UCM fluid with $E = 1$ (see Fig. 19) we observe that the behaviour of the Maxwell fluid differs significantly from the Newtonian one: both the amplitude and the phase of the maximum velocity oscillation are substantially different, for the Stokes number here considered of $\alpha = 4.864$.

In contrast to the start-up test case, it is surprising to verify that for the UCM fluid a mesh with 100 CV is wholly inadequate to yield numerical results close to the theoretical ones, as shown in Fig. 19. This figure reinforces the idea already commented before (Section 5.2) that it is mesh refinement that controls the error. It presents the theoretical variation of the centreline velocity ($Y = 0$ in Eq. (46)) during one period and various numerical solutions. A mesh with 100 CV and time steps of 1×10^{-2} and 1×10^{-3} were employed, together with a more refined mesh with 1000 CV and time step of $\Delta t = 10^{-3}$. Only by using this finer mesh and the refined step in time could we gather sufficient conditions to obtain good agreement between theory and numerical simulations. This is reflected in the velocity profiles presented in Fig. 20 for $\omega t = 0^\circ, 90^\circ, 180^\circ$ and 270° where, for the spatial resolution of 1000 CV, almost no discrepancies between the theoretical solution and numerical results are seen. Fig. 21(a) and (b) shows the corresponding predictions of shear and normal stress components (denoted by various symbols) contrasted against the theoretical solution of Eqs. (47) and (48) (denoted by lines), and there is clearly a good match due to the use of such a refined mesh, in spite of some localised discrepancies (especially for T_{xx}).

Both Figs. 20 and 21 reveal the propagation of short-wave oscillating motions across the channel, and about 8 wave peaks can be counted from either the velocity or stress variations. Thus the wavelength normalized with h is estimated as $1/4$. This estimation can be approximately confirmed from the theoretical solution of Section 4.2; in Eq. (38) the only possible term responsible for spatial wave propagation is $\cosh(zY)$ and for large $\alpha^2 E$ and small β , Eq. (35) gives $z \approx i\alpha^2 \sqrt{E}$. Therefore $\cosh(zY) \approx \cos(\alpha^2 \sqrt{E} Y)$ with wavelength $\ell = 2\pi/\alpha^2 \sqrt{E}$; for the present case we have $E = 1$ and $\alpha = 4.864$, yielding $\ell = 0.265 = 1/3.8$ in agreement with the estimation from the figures.

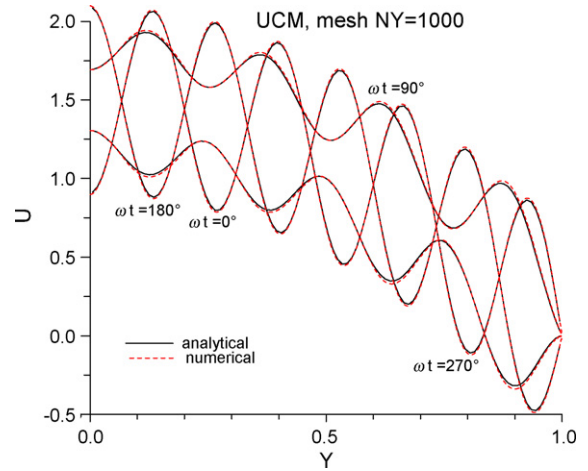


Fig. 20. Velocity profiles of an UCM fluid in the oscillatory regime during one cycle ($\Delta t = 1 \times 10^{-3}$ and $\Delta y = 1 \times 10^{-3}$).

It is well known that the UCM model can be viewed as a particular case of the more general Oldroyd-B model when the retardation time is zero ($\lambda_r = 0$), which is equivalent to the absence of a Newtonian solvent contribution to the total viscosity ($\beta = \eta_s/\eta_0 = 0$). As anticipated, it is easier to find accurate numerical solutions with the Oldroyd-B model than with the UCM. Fig. 22 shows a comparison of the evolution of the centreline velocity with time for Newtonian,

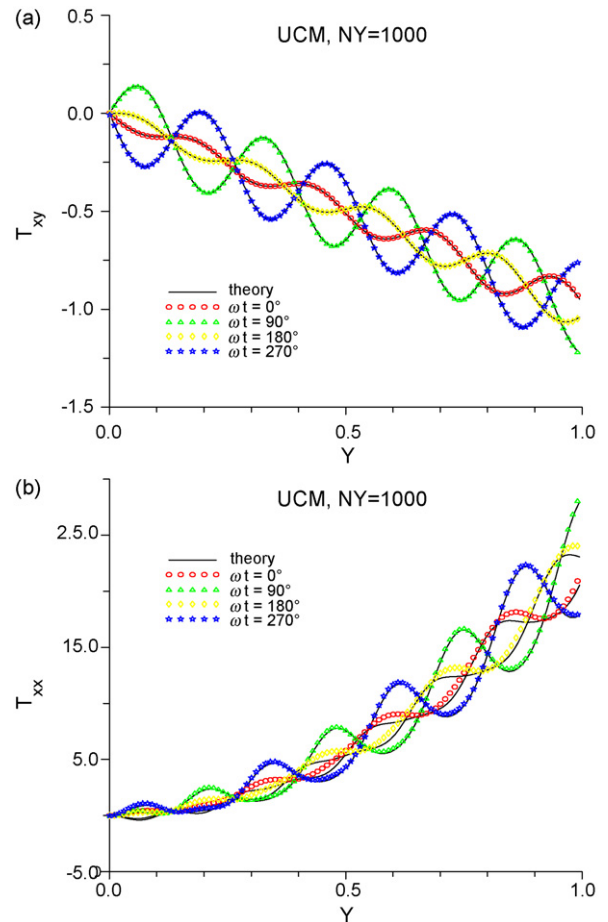


Fig. 21. (a) Shear and (b) normal stress profiles of an UCM fluid in the oscillatory regime during one cycle ($\Delta t = 1 \times 10^{-3}$ and $\Delta y = 1 \times 10^{-3}$).

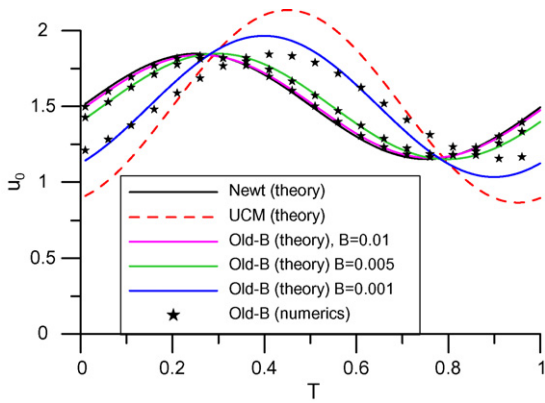


Fig. 22. Evolution of centreline velocity with time for the pulsating flow ($\alpha = 4.864$) of various fluids: Newtonian (theoretical solution); UCM ($E = 1$, theoretical solution); Oldroyd-B ($\beta = 0.01$; 0.005 ; 0.001 ; $E = 1$; lines- theory; symbols- predictions with $\Delta t = 1 \times 10^{-2}$; $\Delta y = 1 \times 10^{-2}$).

UCM and Oldroyd-B ($\beta = 0.01$; 0.005 ; 0.001) fluids. As can be seen from the graph, the Newtonian and Oldroyd-B ($\beta \geq 0.005$) fluids present a similar behaviour which differs significantly in amplitude and phase from that for the UCM fluid. The numerical prediction for the Oldroyd-B fluid with the typical value of $\beta = 0.1$ (recall that the solvent viscosity ratio is often taken as $\beta = 1/9$), or $\beta = 0.01$ shown

in the figure, matches well the analytical solution even when a 100 CV mesh and a time step of 1×10^{-2} are employed, but that is not possible with the UCM model (for which $\beta = 0$).

Some point-wise results using the Oldroyd-B model, showing a comparison between analytical solutions and the predicted velocity profiles obtained by the computer program at four time instants during the oscillatory period, with phase angles $\omega t = 0^\circ, 90^\circ, 180^\circ$ and 270° , are now presented. Fig. 23(a)–(d) show these results for a range of the viscosity parameter $\beta = 0.1, 0.01, 0.005$ and 0.001 . We recall that $\beta = 1$ corresponds to the Newtonian model for which there is no elastic contribution to the stress tensor, while $\beta \rightarrow 0$ leads to the UCM model. The predictions seen in these figures were calculated on MESH 2 ($\Delta y = 1 \times 10^{-2}$) with a time step of $\Delta t = 1 \times 10^{-2}$, which appears adequate at $\beta = 0.1$ and 0.01 , where excellent agreement between analytical and numerical solutions is observed. In contrast, Fig. 23(c) and (d) show velocity profiles for the Oldroyd-B fluid with $\beta = 0.005$ and 0.001 and in these figures some discrepancies between the numerical results and the analytical solution are discernible, reflecting a feature common to all numerical simulations with viscoelastic fluids: amongst all rheological models, the UCM appears as the most problematic and difficult in numerical terms. Difficulties in achieving both iterative convergence and sufficient accuracy found for the Oldroyd-B model, tend to increase as the β value decreases and the UCM model is approached. Then, mesh refinement is mandatory in order to improve the predictions, as demonstrated in Fig. 23 (d) for the

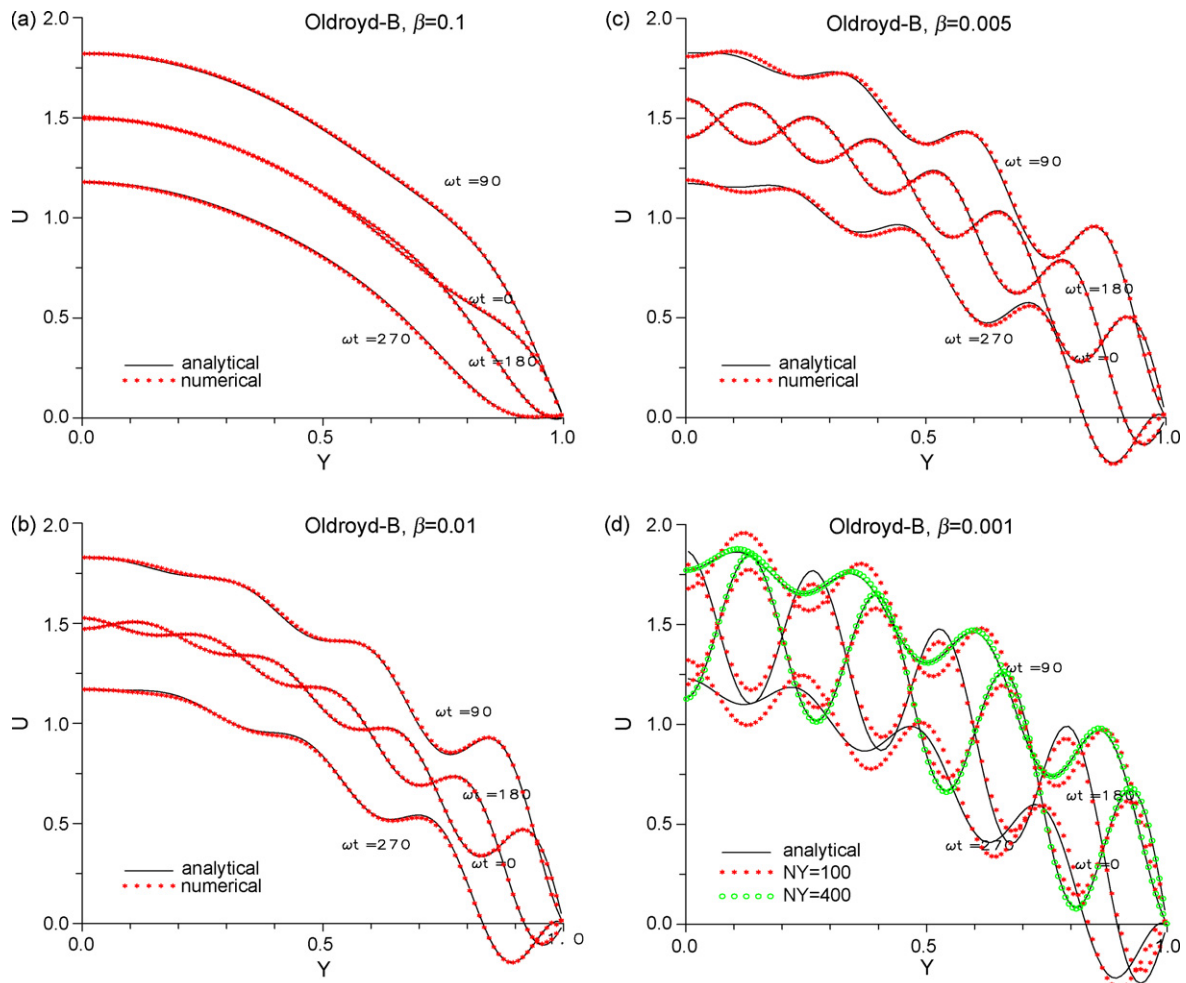


Fig. 23. Velocity profiles of an Oldroyd-B fluid in the oscillatory regime during one cycle ($E = 1$, $\Delta t = 1 \times 10^{-2}$ and $\Delta y = 1 \times 10^{-2}$): (a) $\beta = 0.1$, (b) $\beta = 0.01$, (c) $\beta = 0.005$ and (d) $\beta = 0.001$ (circles- $\Delta y = 0.25 \times 10^{-2}$).

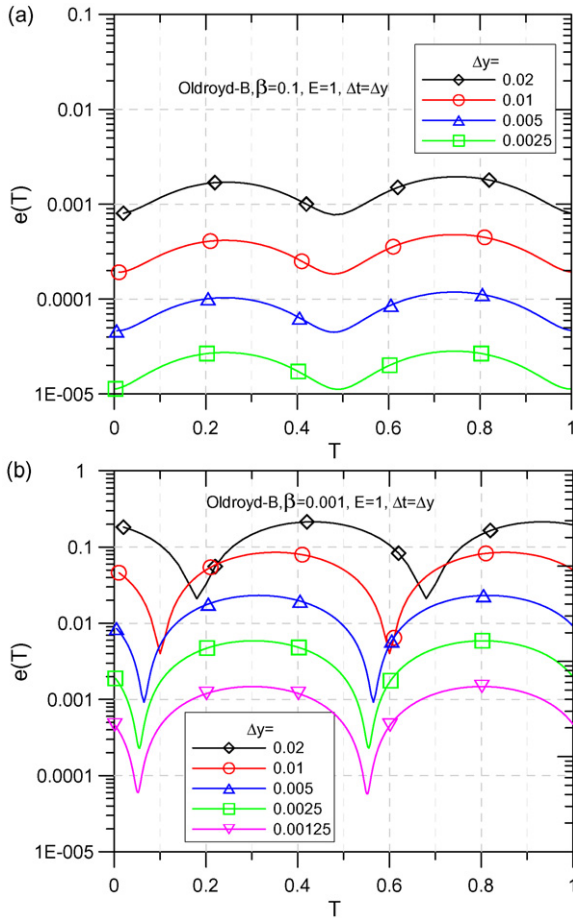


Fig. 24. Evolution of discretization error during one period of the pulsating flow of two Oldroyd-B cases, $\beta=0.1$ and 0.001 ($E=1$), calculated with various meshes and time steps, such that $\Delta t = \Delta y$.

case of $\beta=0.001$ where further predictions with a mesh having $\Delta y=0.25 \times 10^{-2}$ (after doubling twice the number of cells of the base mesh, from $NY=100$ to $NY=400$) are also plotted as round symbols; these fall virtually on the line corresponding to the analytical solution.

The distribution of the discretization error along one period of the imposed oscillations using four different uniform meshes and corresponding smaller time steps is plotted in Fig. 24. Two Oldroyd-B cases are shown, one with the typical value of $\beta=0.1$ and the other with a much smaller $\beta=0.001$, thus very close to a UCM fluid. In general, the error is seen to follow a sinusoidal-like variation during the cycle and, in the log scale shown, it is reduced by a constant amount due to the technique here employed (cf. Section 5.2, Eq. (50)) of simultaneously refining the mesh spatially and the step forward in time in a consistent manner: $\Delta y_1 = \Delta t_1 = 1/50$, $\Delta y_2 = \Delta t_2 = 1/100$, $\Delta y_3 = \Delta t_3 = 1/200$ and $\Delta y_4 = \Delta t_4 = 1/400$. A good “parallelism” between the error variations is observed in Fig. 24(a) for $\beta=0.1$, with a constant separation of about $2 \log 2$ typical of 2nd order accuracy, while in part (b) for $\beta=0.001$ a phase lag is patent, especially for the coarser level of simultaneous mesh and Δt refinement, but the error reduction of 4 is also seen on the finer discretizations (an additional discretization level of $\Delta y_5 = \Delta t_5 = 1/800$ is included in Fig. 24(b) to make this fact clearer). Hence, very small β values in the Oldroyd-B model, and consequently also the UCM model, require even smaller time steps and finer meshes. It is noteworthy that the error for the Oldroyd-B $\beta=0.001$ is smaller than 10^{-3} only for meshes having more than 400 CVs ($\Delta y < 0.0025$) while

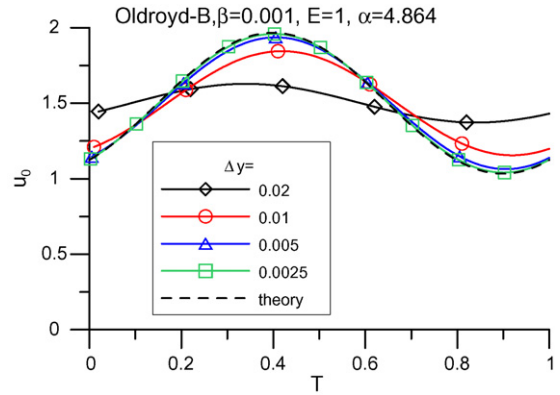


Fig. 25. Convergence of centreline velocity with mesh refinement for the pulsating flow ($\alpha=4.864$) of an Oldroyd-B fluid ($\beta=0.001$; $E=1$): predictions on 4 successively refined levels with $\Delta t = \Delta y$.

if β is increased to 0.1 the mesh $NY=100$ is sufficient to obtain errors bounded by 10^{-3} .

Convergence of the numerical results with mesh refinement is illustrated more directly in Fig. 25, showing the predicted centreline velocity for the Oldroyd-B with $\beta=0.001$ obtained using 4 consistently refined meshes. Starting with $MESH1$, $NY=50$, the number of cells was successively doubled until reaching $NY=400$ and $\Delta y=0.0025$, while the time step was simultaneously halved from the initial value of $\Delta t=0.02$. The conclusions of the previous paragraph regarding the error decay are now plainly seen: for such low value of β maintaining the accuracy of the predictions to within a reasonable error band requires meshes with as much as 400 cells. In addition Fig. 26 shows with symbols the convergence rates obtained for the Oldroyd-B model with $\beta=0.001$ (open squares), $\beta=0.01$ (triangles), $\beta=0.1$ (circles), and the UCM (circular symbols). The data were obtained by integrating the local errors, calculated with Eq. (49), over one period: $e = \sum_0^1 e(T)/NT$ (NT is the corresponding number of time steps). A graphical fitting routine yields rates of $p=1.98$ for the UCM, and for the Oldroyd-B $p=1.98$, 1.99 and 2.01 for $\beta=0.001$, 0.01 and 0.1 , respectively, on the 3 finer discretizations. If all the 5 meshes are taken into account when evaluating the convergence rate, there is a deterioration as β is reduced: $p=2.00$, 2.02 , 1.98 , 1.83 and 1.72 , for $\beta=1.0$, 0.1 , 0.01 , 0.001 and 0.0 , respectively. Although the error decaying rates are almost the same for all cases, when going from the Oldroyd-B model with $\beta=0.1$ to the UCM, the magnitude of the RMS errors for the latter are much

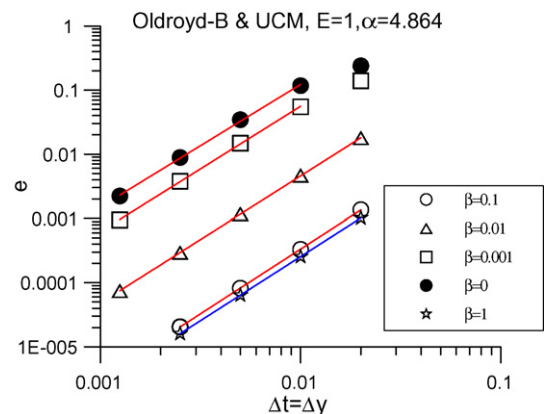


Fig. 26. Convergence plots for the pulsating flow ($\alpha=4.864$, $E=1$) of Oldroyd-B, UCM ($\beta=0$) and Newtonian ($\beta=1$) fluids. Discretization refinement with $\Delta t = \Delta y$. Error e calculated over a period.

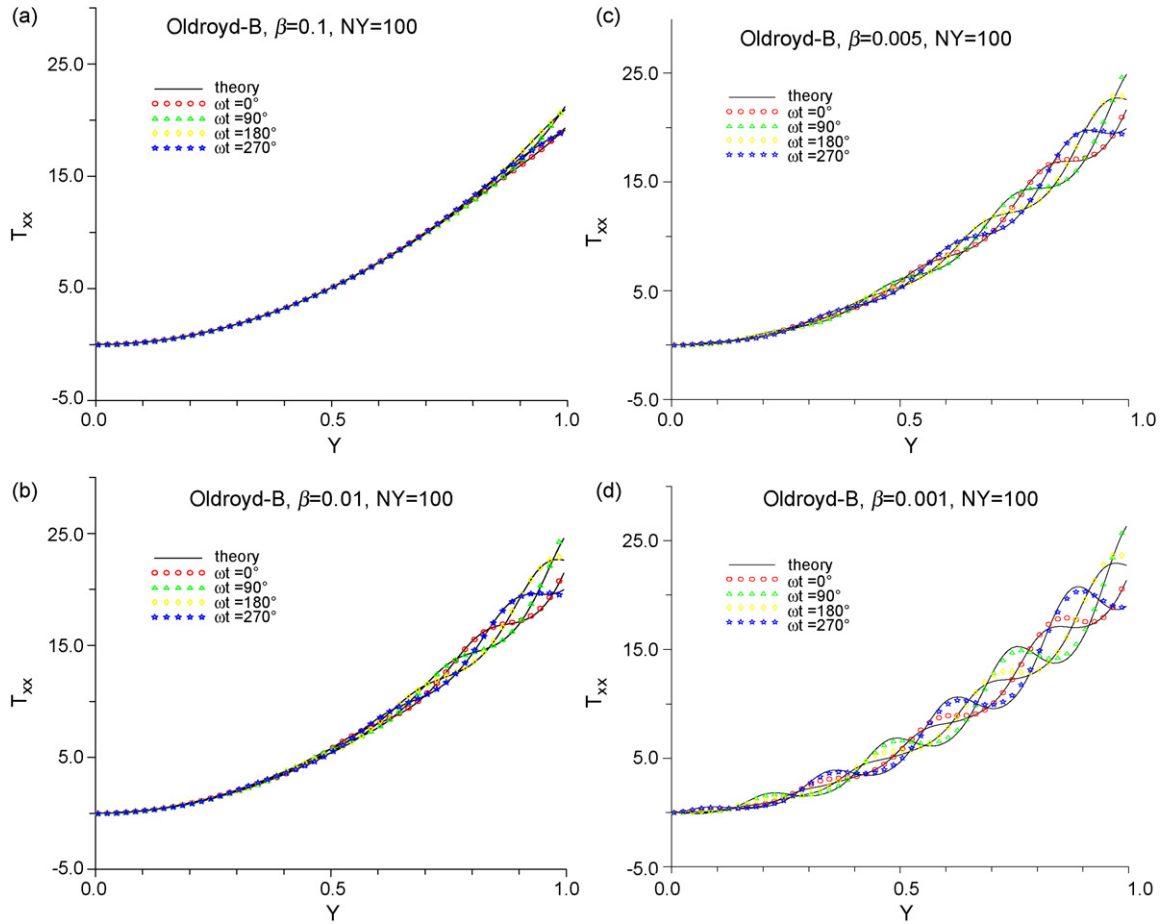


Fig. 27. Normal stress profiles of an Oldroyd-B fluid in the oscillatory regime during one cycle ($E=1$, $\Delta t=1 \times 10^{-2}$ and $\Delta y=1 \times 10^{-2}$): (a) $\beta=0.1$, (b) $\beta=0.01$, (c) $\beta=0.005$ and (d) $\beta=0.001$.

higher (by about 3 orders of magnitude). In conclusion, the overall rate of convergence is about 2 for all the viscoelastic pulsating cases, as in the previous start-up problem, except that in that case the UCM showed a 1st order convergence due to the discontinuous character of the shear waves generated. However, the rate of convergence is not the only useful information from Fig. 26: it also reveals that the UCM model requires a discretization of order 10^{-3} to get the same error magnitude of the Oldroyd-B having $\beta=0.1$ at a discretization $\approx 2 \times 10^{-2}$.

In terms of stress predictions Fig. 27(a)–(d) shows the normal stress profiles at four time instants during the oscillatory period and a comparison between analytical results and numerical solutions for β values ranging from 0.1 to 0.001. Analogous features to the ones already commented upon in relation to the velocity profiles (Fig. 23(a)–(d)) are patent in these figures. This point is made even clearer in Fig. 22 above, where we observe the approach of the Oldroyd-B fluid results to the UCM ones when β decreases and tends to 0. A degradation of the accuracy of the results is also observed on the mesh with 100 CV especially as β becomes lower than 0.005.

Regarding the short-wave propagation across the channel, it is interesting to notice by comparing Fig. 27 against Fig. 23 that the wavelength is the same as for the UCM fluid, therefore being independent of β as the above analysis showed. About the same 8 peaks are observed in these figures. When β increases, wave propagation is killed because z now tends to $z \approx \sqrt{i\alpha}/\sqrt{\beta}$ and the $\cosh(zY)$ does not lead to a sinusoidal function (either a sinus or a co-sinus).

6. Conclusions

In this paper, numerical and analytical modelling of time-dependent viscoelastic fluid flow was addressed. In particular, one important test case for the assessment of computational simulation programs was proposed and its theoretical solution derived.

Initially the start-up planar Poiseuille flow test case was analysed. Comparison between Newtonian and UCM fluids showed different behaviour during the transient regime before reaching a steady state, with an oscillatory response for the UCM. It was also verified that the Maxwell fluid took longer to attain a steady state, more so as the elasticity number was increased and the period of the physical oscillations decreased. Small numerical oscillations were present next to the locations where a discontinuity of the time derivative would physically occur. Besides that, the results obtained were sufficiently accurate to predict the shear wave propagation along time with an almost exact prediction of the instants in time when those “shocks” generated at each wall passed through the channel centreline and interfere with each other, giving rise to strong error oscillations. With the Oldroyd-B model we observed a smoother development of the transient evolution and of the spatial variation of the flow field, as already reported in previous studies [5,8,10]. The actual rate of convergence of our method was verified to be 2 for all the Oldroyd-B cases studied ($\beta=0.1-0.001$) and decreasing to 1 for the UCM model.

For the PTT model without a solvent viscosity, behaviour similar to that produced by the UCM fluid was observed but due to the shear-thinning viscosity implied in the PTT equation, the stationary

state was attained quicker. For the FENE-CR fluid the behaviour observed was similar to that found for the Oldroyd-B fluid but in this case there was a reduction in the oscillatory frequency of the response as well as an attenuation of the peak of the oscillation.

For the pulsating viscoelastic flow case, the most interesting of the two considered, some similar and some new conclusions could be drawn. Good agreement between theoretical and numerical solutions could be observed for the Newtonian fluid under steady and unsteady regimes but the viscoelastic fluids showed very different behaviour. While for the Oldroyd-B fluid there was no trouble in obtaining accurate results for $\beta > 0.005$ using reasonable meshes and time steps (of order 0.01), the accuracy would deteriorate as β became smaller and the UCM model was approached, in spite of having established 2nd order convergence rate for all pulsating flow cases (including the UCM). For this latter model very fine meshes were required ($\Delta y = 1/1000$) together with very small time steps ($\Delta t = 1/1000$). Even for a low elasticity number of $E = 1$ the UCM model, possessing no purely viscous dissipation, tended to develop short-wave pulses propagating across the channel and such local phenomena seem to require very tight resolution. The pulsating planar channel problem with the UCM model is thus a most adequate test case for assessment of viscoelastic codes under unsteady flow conditions. This test flow offers some advantages in comparison to the start-up flow:

- it is periodic instead of transient, therefore being less sensitive to the exact initial conditions and thus enabling a check on the repeatability of the numerical solution at every period;
- it does not generate “shocks” that lead to the propagation of velocity-gradient discontinuities, which are harmful because high-order numerical schemes tend to loose accuracy near those points;
- hence, the control of discretization errors and convergence rate of the method can be done much more effectively.

Acknowledgement

The authors would like to thank the financial support given by Fundação para a Ciência e Tecnologia (FCT), Portugal, through the project POCTI/EME/48665/2002.

References

- [1] R. Keunings, Simulation of viscoelastic flow, in: C.L. Tucker (Ed.), *Computer Modeling for Polymer Processing*, Hauser, Munich, 1989.
- [2] F.T.P. Baaijens, Mixed finite element methods for viscoelastic flow analysis: a review, *J. Non-Newtonian Fluid Mech.* 118 (2004) 83–101.
- [3] G. Mompean, M. Deville, Unsteady finite volume simulation of Oldroyd-B fluid through a three-dimensional planar contraction, *J. Non-Newtonian Fluid Mech.* 72 (1997) 253–279.
- [4] P.J. Oliveira, Method for time-dependent simulations of viscoelastic flows: vortex shedding behind cylinder, *J. Non-Newtonian Fluid Mech.* 101 (2001) 113–137.
- [5] S.C. Xue, R.I. Tanner, N. Phan-Thien, Numerical modelling of transient viscoelastic flows, *J. Non-Newtonian Fluid Mech.* 123 (2004) 33–58.
- [6] O.G. Harlen, J.M. Rallison, P. Szabo, A split Lagrangian–Eulerian method for simulating transient viscoelastic flows, *J. Non-Newtonian Fluid Mech.* 60 (1995) 81–104.
- [7] T. Sato, S.M. Richardson, Explicit numerical simulation of time-dependent viscoelastic flow problems by a finite element/finite volume method, *J. Non-Newtonian Fluid Mech.* 51 (1994) 249–275.
- [8] M.F. Webster, H.R. Tammadon-Jahromi, M. Aoubacar, Transient viscoelastic flows in planar contractions, *J. Non-Newtonian Fluid Mech.* 118 (2004) 83–101.
- [9] N. Fietier, M.O. Deville, Time-dependent algorithms for the simulation of viscoelastic flows with spectral element methods: applications and stability, *J. Comput. Phys.* 186 (2003) 93–121.
- [10] R.G.M. Van Os, T.N. Phillips, Spectral element methods for transient viscoelastic flow problems, *J. Comput. Phys.* 201 (2004) 286–314.
- [11] P. Wapperon, R. Keunings, V. Legat, The backward-tracking Lagrangian particle method for transient viscoelastic flows, *J. Non-Newtonian Fluid Mech.* 91 (2000) 273–295.
- [12] R.A. Keiller, Numerical instability of time-dependent flows, *J. Non-Newtonian Fluid Mech.* 43 (1992) 229–246.
- [13] R.A. Keiller, Spatial decay of steady perturbations of plane Poiseuille flow for the Oldroyd-B equation, *J. Non-Newtonian Fluid Mech.* 46 (1993) 129–142.
- [14] P.J. Oliveira, F.T. Pinho, G.A. Pinto, Numerical simulation of non-linear elastic flows with a general collocated finite volume method, *J. Non-Newtonian Fluid Mech.* 79 (1998) 1–43.
- [15] M. Ellero, R.I. Tanner, SPH simulations of transient viscoelastic flows at low Reynolds number, *J. Non-Newtonian Fluid Mech.* 132 (2005) 61–72.
- [16] F.M. White, *Fluid Mechanics*, McGraw-Hill, 1999.
- [17] N.D. Waters, M.J. King, Unsteady flow of an elastico-viscous liquid, *Rheol. Acta* 9 (1970) 345–355.
- [18] R. Keunings, On the high Weissenberg number problem, *J. Non-Newtonian Fluid Mech.* 20 (1986) 209–216.
- [19] N. Phan-Thien, A non-linear network viscoelastic model, *J. Rheol.* 22 (1978) 259–283.
- [20] N. Phan-Thien, R.I. Tanner, A new constitutive equation derived from network theory, *J. Non-Newtonian Fluid Mech.* 2 (1977) 353–365.
- [21] R.B. Bird, R.C. Armstrong, O. Hassager, *Dynamics of Polymeric Liquids. Volume II. Kinetic Theory*, John Wiley & Sons, New York, 1987.
- [22] M.D. Chilcott, J.M. Rallison, Creeping flow of dilute polymer solutions past cylinders and spheres, *J. Non-Newtonian Fluid Mech.* 29 (1988) 381–432.
- [23] R.B. Bird, W.E. Stewart, E.N. Lightfoot, *Transport Phenomena*, John Wiley & Sons, New York, 1960.
- [24] K.D. Rahaman, H. Ramkissoon, Unsteady axial viscoelastic pipe flows, *J. Non-Newtonian Fluid Mech.* 57 (1995) 27–38.
- [25] T. Manos, G. Marinakis, S. Tsangaris, Oscillating viscoelastic flow in a curved duct—exact analytical and numerical solution, *J. Non-Newtonian Fluid Mech.* 135 (2006) 8–15.
- [26] R.G. Owens, A new microstructure-based constitutive model for human blood, *J. Non-Newtonian Fluid Mech.* 140 (2006) 57–70.
- [27] J.M. Khodadadi, N.S. Vlachos, D. Liepsch, S. Moravec, LDA measurements and numerical prediction of pulsatile laminar flow in a plane 90-degree bifurcation, *J. Biomech. Eng.* 110 (1988) 129–136.
- [28] T. Hayat, A.M. Siddiqui, S. Asghar, Some simple flows of an Oldroyd-B fluid, *Int. J. Eng. Sci.* 39 (2001) 135–147.